

Rheology and Structure of Model Smectite Clay: Insights from Molecular Dynamics

Zhu-Yuan Lin¹ and Takahiro Hatano¹

¹Osaka University

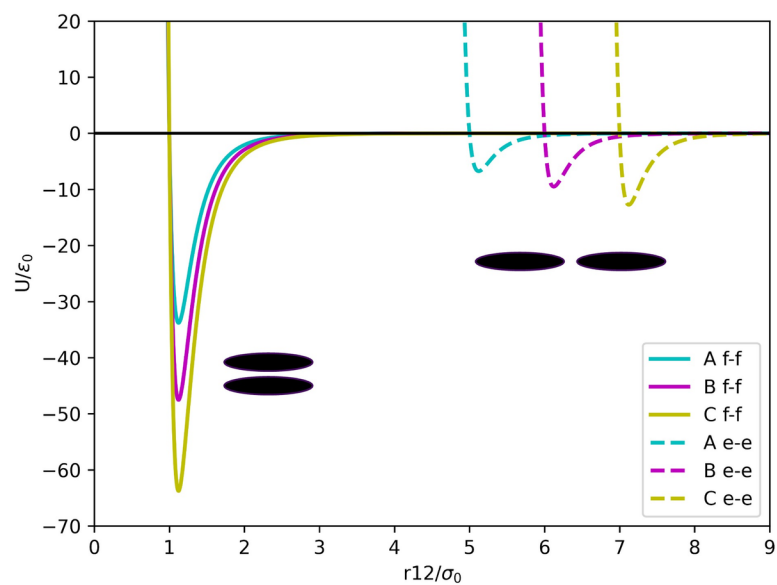
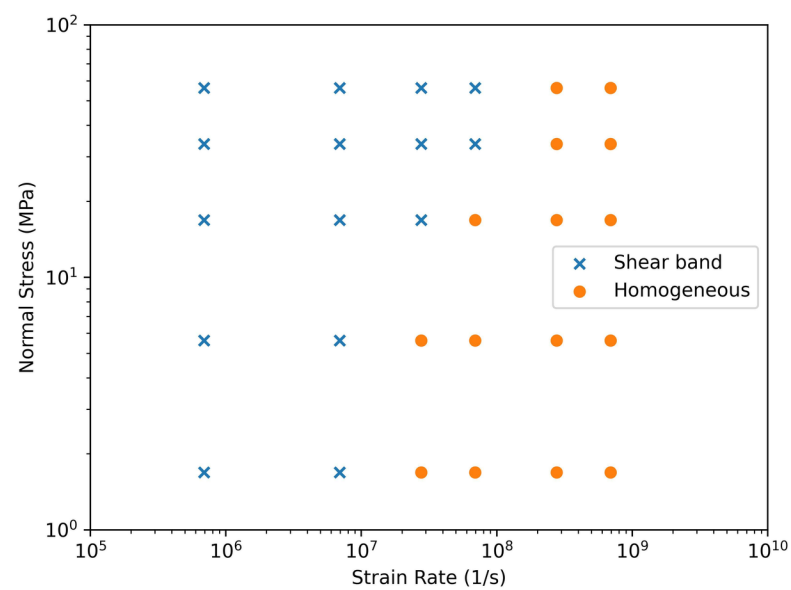
April 16, 2024

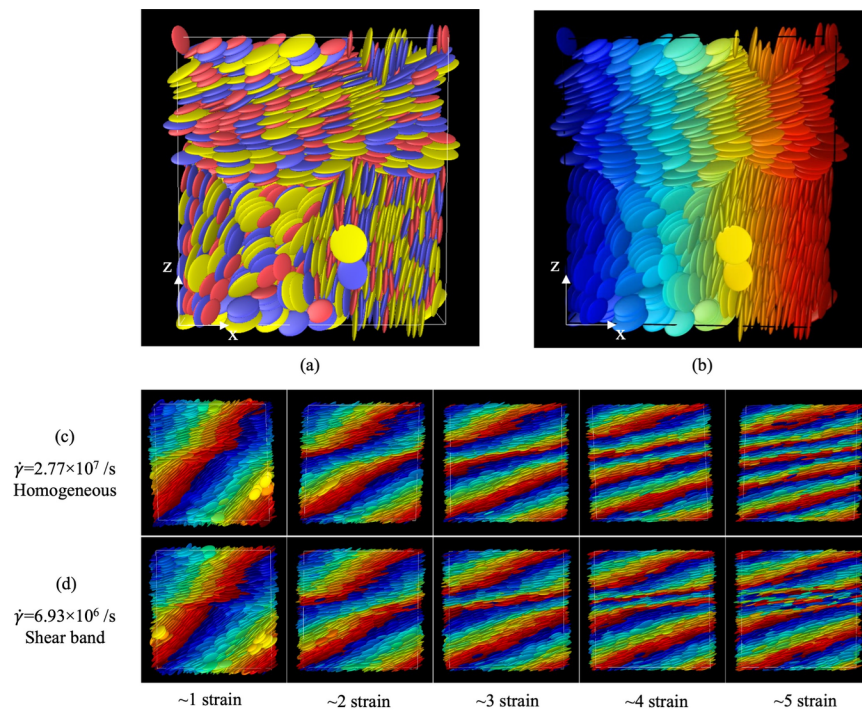
Abstract

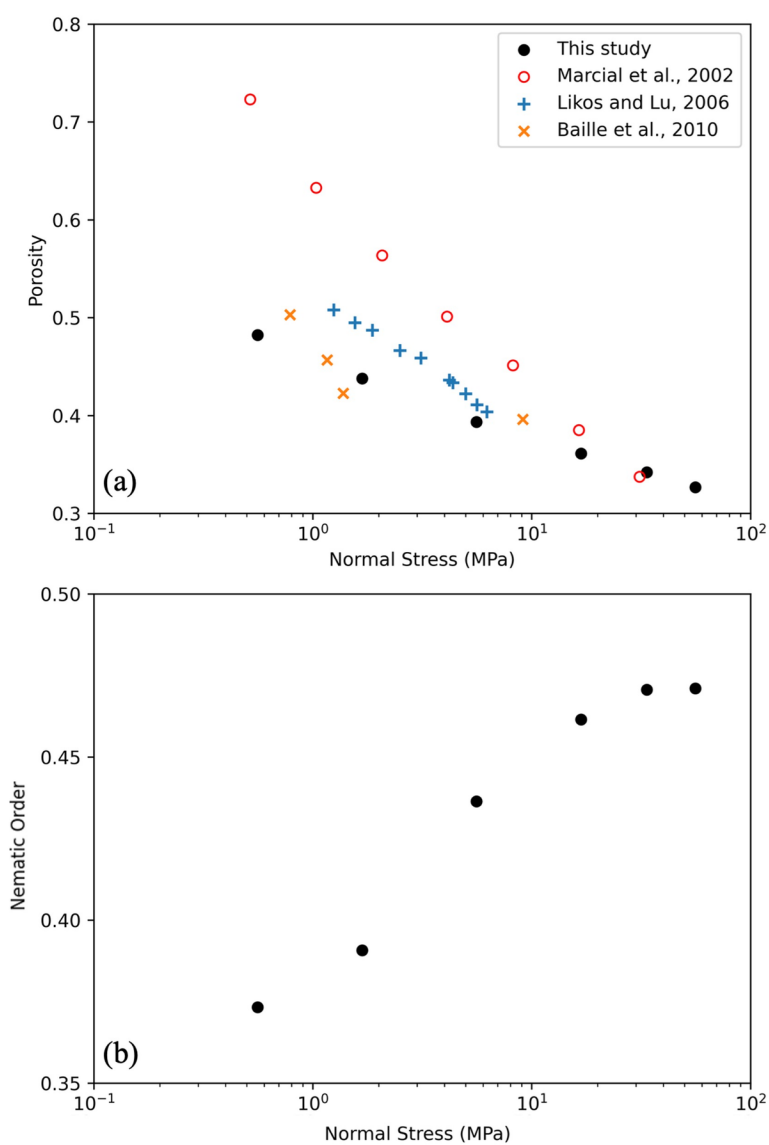
The low frictional strength of smectite minerals such as montmorillonite is thought to play a crucial role in controlling the rheology and the stability of clay-rich faults. In this study, we perform coarse-grained molecular dynamics simulations on a model clay system, in which clay platelets are simplified as oblate ellipsoids interacting via Gay-Berne potential. We study the rheology and the structure development during shear in this model system, which is sheared at constant strain rates for 10 strains after compression and equilibrium. We find that the system exhibits velocity-strengthening behavior over a range of normal stresses from 1.68 to 56.18 MPa and a range of strain rates from 6.93×10^5 to 6.93×10^8 /s. The relationship between the shear stress and the strain rate follows the Herschel-Bulkley model. In general, shear is localized at lower strain rate and higher normal stress, whereas the homogeneous shear is realized at higher strain rates. The structure change by the shear is analyzed from various aspects: the volume fraction, the particle orientation, the velocity profile, and the parallel radial distribution function. We find that particle rearrangement and compaction dominate at the early stage of shear when the shear stress increases. Shear band starts to form at the later stage when the shear stress decreases and relaxes to a steady-state value. The structure development at low strain rates is similar to that in previous experimental observations. The stacking structure weakens during shear, and restores logarithmically with time in the rest period.

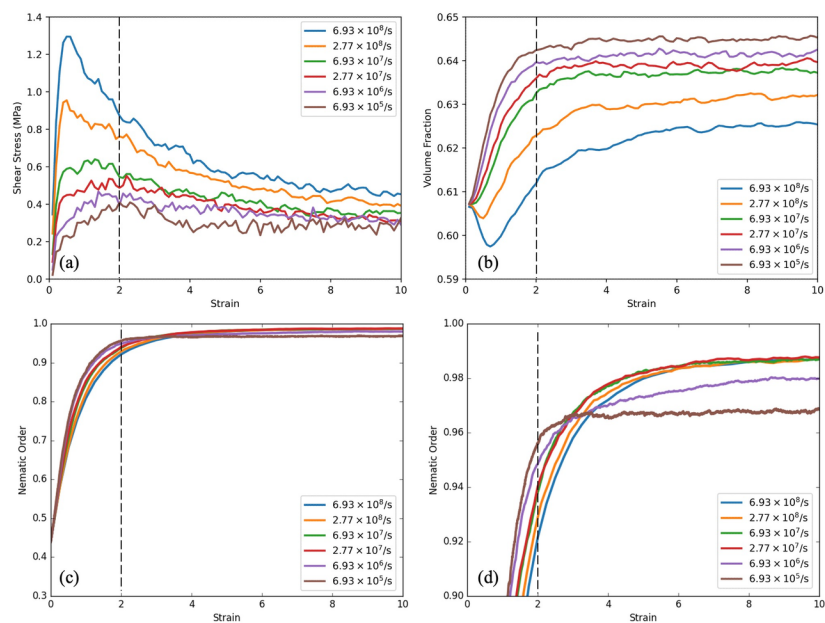
Hosted file

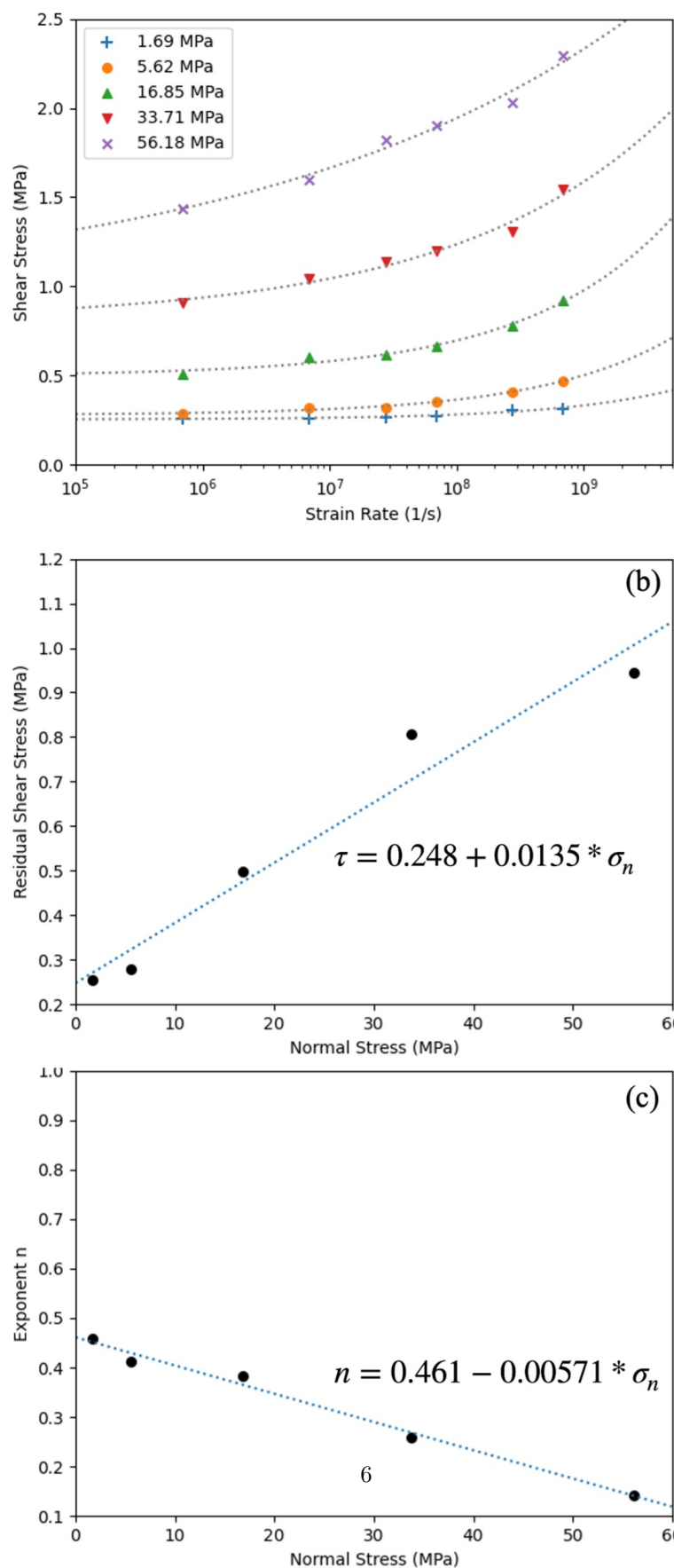
Lin_Feb1_article.docx available at <https://authorea.com/users/722967/articles/714631-rheology-and-structure-of-model-smectite-clay-insights-from-molecular-dynamics>

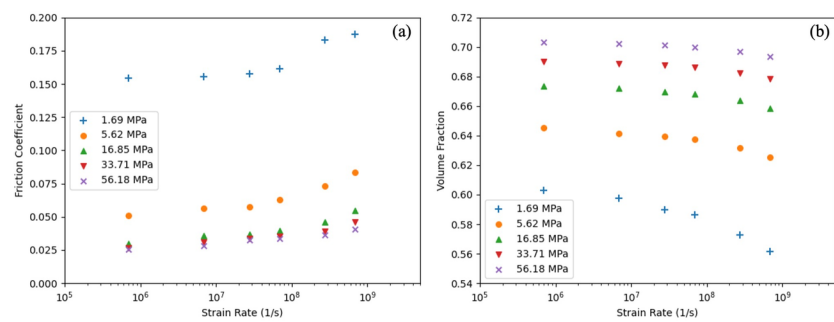


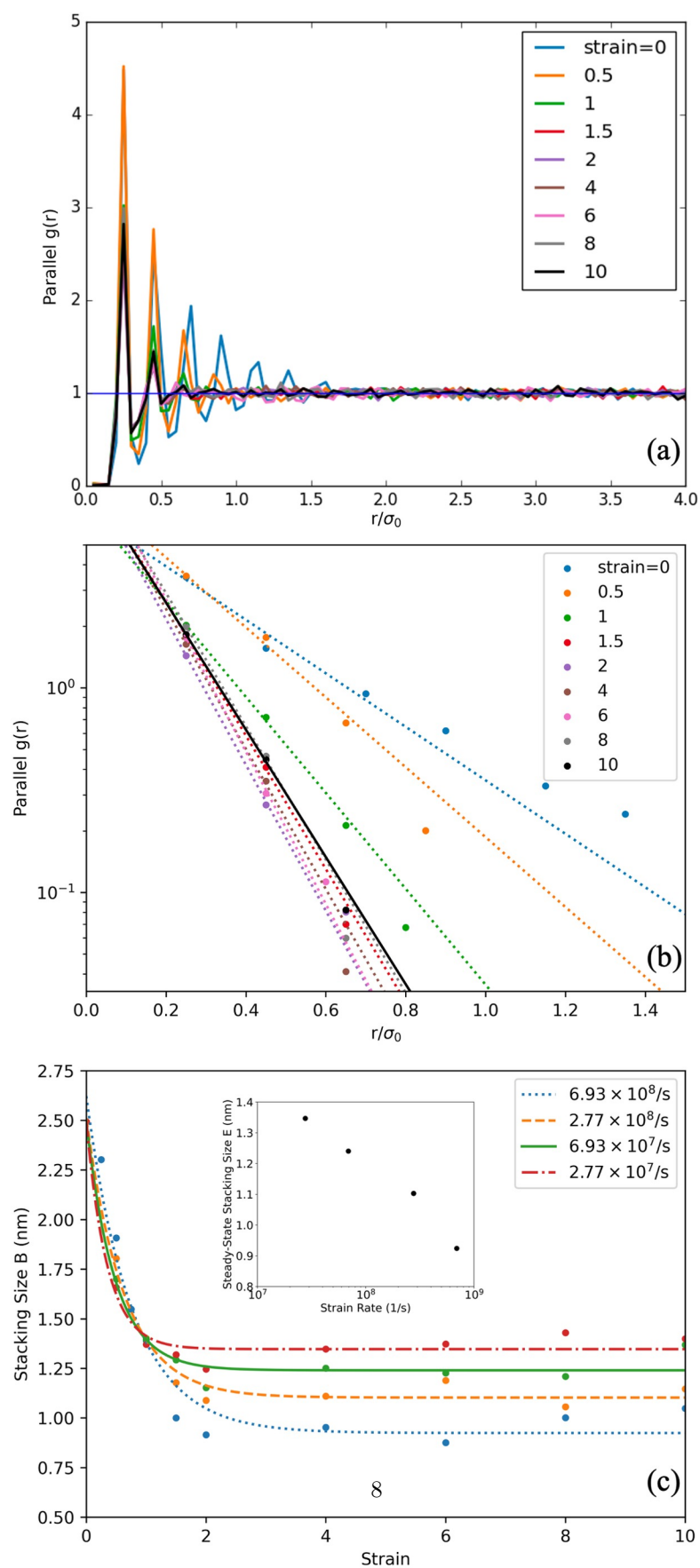


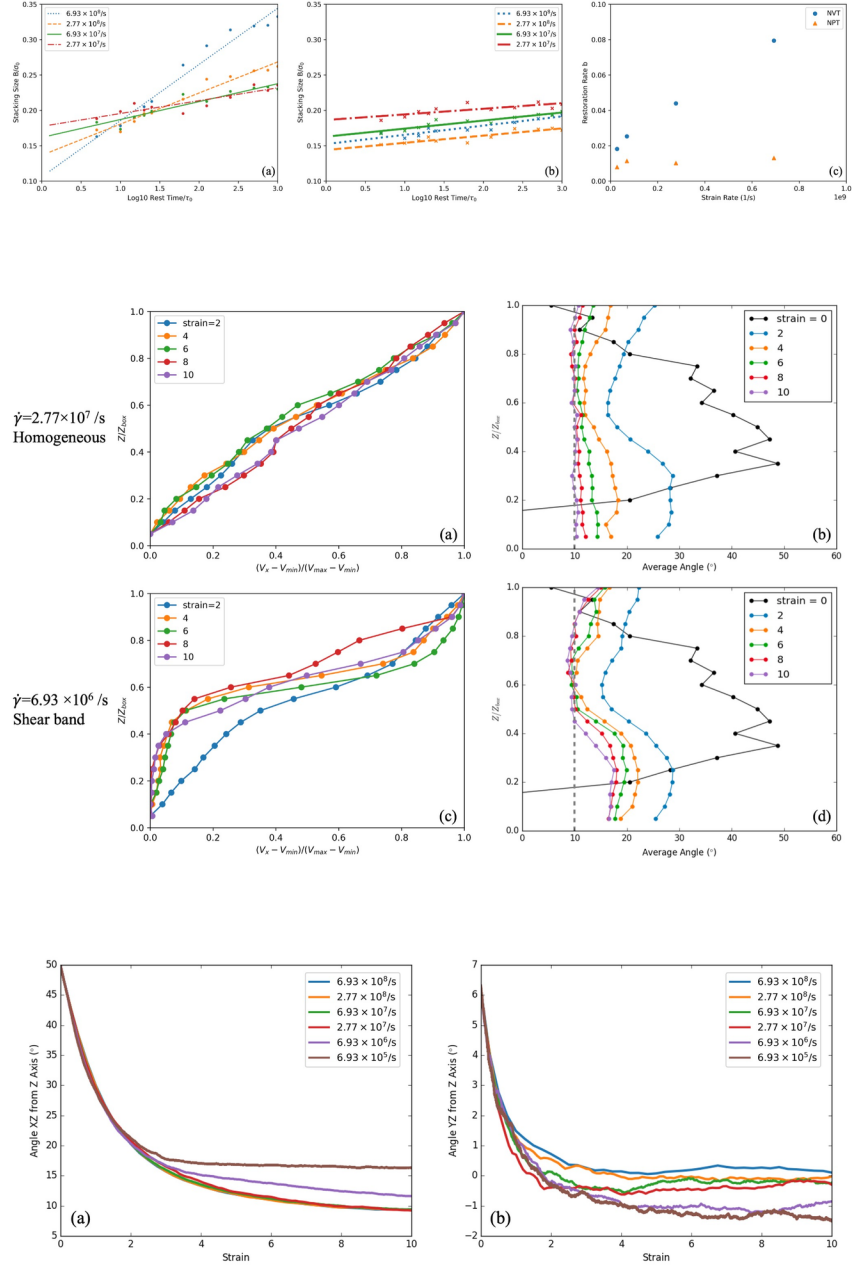












Rheology and Structure of Model Smectite Clay: Insights from Molecular Dynamics

Z.-Y. Lin¹ and T. Hatano¹

¹Department of Earth and Space Science, Osaka University, Osaka, Japan

Corresponding author: Zhu-Yuan Lin (lin@neq.ess.sci.osaka-u.ac.jp)

Key Points:

- A model clay system shows velocity-strengthening behavior following the Herschel-Bulkley model.
- Particle rearrangement and compaction dominate at early strains followed by shear band formation at low strain rate.
- The stacking structure of clay platelets weakens during shear and undergoes logarithmic healing with time in the system at rest.

Abstract

The low frictional strength of smectite minerals such as montmorillonite is thought to play a crucial role in controlling the rheology and the stability of clay-rich faults. In this study, we perform coarse-grained molecular dynamics simulations on a model clay system, in which clay platelets are simplified as oblate ellipsoids interacting via Gay-Berne potential. We study the rheology and the structure development during shear in this model system, which is sheared at constant strain rates for 10 strains after compression and equilibrium. We find that the system exhibits velocity-strengthening behavior over a range of normal stresses from 1.68 to 56.18 MPa and a range of strain rates from 6.93×10^5 to 6.93×10^8 /s. The relationship between the shear stress and the strain rate follows the Herschel-Bulkley model. In general, shear is localized at lower strain rate and higher normal stress, whereas the homogeneous shear is realized at higher strain rates. The structure change by the shear is analyzed from various aspects: the volume fraction, the particle orientation, the velocity profile, and the parallel radial distribution function. We find that particle rearrangement and compaction dominate at the early stage of shear when the shear stress increases. Shear band starts to form at the later stage when the shear stress decreases and relaxes to a steady-state value. The structure development at low strain rates is similar to that in previous experimental observations. The stacking structure weakens during shear, and restores logarithmically with time in the rest period.

Plain Language Summary

The smectite clay minerals have a relatively lower frictional strength comparing to other geomaterials. The strength and stability of clay-rich faults is dependent on the shear behavior of clay minerals. In this study, we perform a series of simulations to study the shear behavior and structure of a simple clay model. The complicate shape and interactions of natural clay are simplified as disc-like ellipsoid and a generalized potential. The system is sheared at constant strain rate for 10 strains after compression and relaxation. The simulations focused on the effect of normal stress and strain rate on shear stress and clay structure. We find that the shear stress increases with strain rate for all tested conditions. Two shear scenarios are observed with shear localization in a narrow region at low strain rate while the shear is homogeneous at high strain rate. The structure development at low strain rates is similar to that in previous experimental observations. We observed the stacking structure of clay platelets weakens during shear. In the rest period after shear, the stacking structure restores in a logarithmic form with rest time and can be associated with the healing of clay-rich fault.

1 Introduction

Smectite minerals, such as montmorillonite, are abundant in the top part of the upper crust and are commonly found in shallow subduction zones (Carpenter et al., 2011; Collettini et al., 2019; Deng and Underwood, 2001; Ikari et al., 2011; Jeppson and Tobin 2015; Lockner et al., 2011; Wojatschke et al., 2016; Wu et al., 1975). During the March 2011 Tohoku-Oki earthquake, the large slip in the shallow part of subduction zone caused a devastating tsunami (Chester et al., 2013; Ujiie et al., 2013). Drilling investigation revealed a clay-rich fault zone with composition of 60~80% smectite (Kameda et al., 2015). The shear resistance of smectite is generally lower than other geomaterials, and therefore it has been linked to the weakness of some specific faults as well as shallow subduction plate boundaries.

Montmorillonite, a typical smectite at low temperatures, consists of platelets with the high aspect ratio and the thickness of ~1 nm. Natural montmorillonite platelets are highly poly-

dispersed in diameter with irregular shapes (Michot et al., 2004). This mineral is well known for its high reactivity to water. In aqueous environment, montmorillonite absorbs and exchanges cations, and the surface of platelets is charged negatively. The charge of platelet edges depends on the ionic condition: they are charged negatively under alkaline condition but charged positively under acidic condition (Paineau et al., 2013). Water molecules are also attracted to the surface and form a few (one to three) crystalline hydrate layers, which contribute to interlayer swelling (Ho et al., 2019; Shen and Bourg, 2021).

The rheology and the stability of fault zone is governed by the mechanical properties of fault gouges. Thus, the frictional strength and the fabric development in clay and simulated fault gouges with various clay contents have been extensively studied in friction experiments (Behnsen and Faulkner, 2013; Bird, 1984; Brown et al., 2003; Haines et al., 2013; Ikari et al., 2007; Moore and Lockner, 2007; Morrow et al., 1992; Saffer and Marone, 2003; Summers and Byerlee, 1977; Tembe et al., 2010; Tesei et al., 2012). The saturation status of sample and the corresponding experimental procedures are crucial to the measurement of frictional properties of montmorillonite, as summarized in Morrow et al. (2017). The friction coefficient increases with the effective normal stress when the montmorillonite is fully saturated with the controlled pore pressure. For other cases including dry, unsaturated, or overpressurized cases, the friction coefficient decreases with the normal stress.

Both the field and the laboratory studies revealed some interesting fabric evolution that may affect the frictional strength of clay-rich faults (Haines et al., 2013; Kenigsberg et al., 2019; Kenigsberg et al., 2020; Logan and Rauen Zahn, 1987; Niemeijer et al., 2010; Saffer and Marone, 2003). For instance, scaly clay foliation is observed in a core sample taken from the shallow source of the 2011 Tohoku-Oki earthquake (Chester et al., 2013). Laboratory experiments using crushed montmorillonite produced Riedel shears and boundary-parallel shears, which were developed systematically with the shear strain (Kenigsberg et al., 2019). SEM observation suggested that clay particles were reoriented on the plane perpendicular to the maximum principal stress (Haines et al., 2013).

In theoretical and simulation studies, a classical description of clay interactions is based on the Derjaguin–Landau–Verwey–Overbeek (DLVO) theory for charged parallel planes. A primitive model (Pellenq et al., 1997) describes the ion density fluctuation between two plates, which is neglected in the DLVO model. This force contributes to the attraction between clay particles with the same charge and leads to parallel stacking of platelets.

Over the last few decades, the understanding on parallel stacking and swelling of clay platelets is greatly improved due to the development of molecular dynamics. The force field of clay can be reproduced with the explicit atomistic clay structure together with the ions and the solvent molecules. However, such fully atomistic modeling is limited to small systems due to the high computational cost (Underwood and Bourg, 2020). For instance, a typical simulation on clay swelling or the interlayer sliding behavior includes only two clay platelets in the bulk water (Ho et al., 2019; Wei et al., 2021).

Attempts have been made to simplify the complicated interactions between clay platelets with the large aspect ratio. For early exploration, an infinitesimally thin disk with a quadrupole potential is used as a clay platlet with the electric double layers (Dijkstra et al., 1995). The following attempt is to construct a platelet from multiple spheres together with some charged sites interacting via Coulomb or Yukawa type of electrostatic potential (Delorme et al., 2014;

Kutter et al., 2000; Odriozola et al., 2004; Ruzicka et al., 2010). The resulting interaction can be viewed as a generalization of DLVO potential for platelets. The aforementioned models mainly focus on dilute dispersion of synthetic clay at low volume fraction. More recent simulations adopted a Lennard-Jones like potential or the DLVO potential (Aminpour and Sjoblom 2019; de Bono et al., 2022; Thrusson et al., 2017). In particular, the Gay-Berne (GB) potential has been used to study clay aggregation (Bandera et al., 2021; Ebrahimi et al., 2014). The GB potential is commonly used in liquid crystal studies and is capable of accounting for both the shape and the interaction anisotropy of clay platelets. The face-to-face and edge-to-edge configuration are considered independently when calibrating the potential parameters using a full-atomistic simulation or the DLVO model.

Coarse-grained simulations have been proved to be a useful tool in recent studies on compressed clay systems (Asadi et al., 2022; Bandera et al., 2021; Bayesteh et al., 2021; de Bono et al., 2022; Ebrahimi et al., 2016). However, in contrast to the experimental approach, few studies have utilized this method to study the rheology or friction of clay under large deformation. Yamamoto et al. (2005) studied the suspension rheology of disk-like particles under simple shear using the GB potential and the Brownian Dynamics. This study predicts the shear-thinning behavior in viscosity and the particle alignment in the flow direction at high strain rate. To consider clay in a fault zone condition, however, a system at higher volume fraction and higher normal stress must be studied.

In this paper, we report the coarse-grained molecular dynamics (CGMD) simulation of a simple model clay from a mesoscopic point of view. We aim to give some insights on the rheology and the structure of clay and clay-rich fault gouges using simple non-sphere particles with the Gay-Berne potential. We focus on the influence of strain rate and normal stress on shear behavior at room temperature. Another aim is to provide some direct evidences on the connection between the shear and the microstructure. To this end, the structure development during shear is probed from volume fraction, particle orientation, velocity profile, and parallel radial distribution function.

2 Materials and Methods

2.1 Outline

The simulations are carried out using the LAMMPS simulation package (Brown et al., 2009; Thompson et al., 2022). The molecules are visualized using the OVITO software (Stokowski, 2009).

Smectite clay platelets are simplified as rigid oblate ellipsoids interacting via the Gay-Berne potential (Coussaert and Baus, 2002; Gay and Berne, 1981; Luckhurst and Simmonds, 1993). The mixture considered in this work consists of three types of ellipsoid with the same population. This poly-dispersity is introduced in order to avoid crystallization and to resemble the structure of natural clay. The non-spherical particles are characterized by the different aspect ratio of 1/5, 1/6, and 1/7 with the same thickness and different diameters (particle type A, B, and C).

The equilibrium phases of this kind of polydisperse ellipsoids must be rich in diversity, but they are not thoroughly understood (Cienega-Cacerez et al., 2016). In our study, particles with the larger aspect ratio have the deeper potential well and therefore they are more likely to stack on each other. However, no apparent crystallization is found by visual inspection.

2.2 Gay-Berne potential

The parameters for the GB potential are chosen so that the potential well between two clay platelets is comparable with the free energy estimate using the full atomistic MD results. However, the full MD results may depend on the specific setup of simulation system, the form of potential function, and the choice of fitting parameters (Ebrahimi et al., 2014). For simplicity, here we do not pursue the perfect match with the full atomistic MD results, but use the values assumed in some recent MD studies.

Based on a MD study on the interaction between two montmorillonite platelets of diameter of ~ 6 nm (Shen and Bourg, 2021), in the present study, the potential well of ~ 0.5 eV is chosen for the face-face interaction of particles with the aspect ratio $\kappa = 1/5$. This value corresponds to the two-layer crystalline hydrates at d-spacing of 1.55 nm in the salinity of 0.3–0.5M NaCl. The ratio of the potential well depth of end-to-end and that of face-to-face is set to 1/5 for all the particles. The soft contact distance is also defined from $\sigma_{A,ff} = \sigma_0 = 1.5$ nm. Particles with aspect ratio of 1/5, 1/6 and 1/7 then correspond to ellipsoids with thickness of 1.5 nm and diameter of 7.5, 9, 10.5 nm, respectively. The set of potential functions is shown in Figure 1. More details on the GB potential are presented in the supporting information.

Note that the potential functions adopted in this study incorporate the effect of solvent and ions implicitly. However, any hydrodynamic effects are not considered. Therefore, the structural changes in the hydrate layers around clay particles by the shear cannot be captured. The swelling and non-swelling component of the stress cannot be discriminated. We assume a fully saturated and fully drained system. Thus, the normal stress in the present simulation should be interpreted as the effective normal stress.

2.3 Configuration and setup of simulation

The simulation is performed using 4096 particles inside a triclinic box with periodic boundary conditions. Translational and rotational equations of motion are integrated using the velocity Verlet algorithm with a reduced time step $\delta t^* = 0.00025$ if not specified. To optimize the computational time, the interaction potentials are truncated at a cutoff of $1.6\sigma_0$.

Initially, each platelet is placed on a simple cubic lattice with the number density of 0.2. The initial orientation and the initial velocity is assigned randomly. For the following time evolution, Langevin thermostat is used to control the temperature at $T^* = 1.75$ (equivalent to 300.41K). In the earliest stage of time evolution (duration of $t^* = 1000$), the system evolves in the NVT ensemble to randomize the platelet configuration. Subsequently, the system is compressed and equilibrated in the NPT ensemble. Nosé-Hoover barostat is used for the pressure control with the normal stresses in the X, Y, and Z directions controlled independently. The target values are $P^* = 100, 300, 1000, 3000, 6000, \text{ and } 10000$ (0.56, 1.69, 5.62, 16.85, 33.71, and 56.18 MPa). For each stage of pressure elevation, the pressure first increases linearly in $t^* = 200$ and is kept constant in the subsequent equilibration process of $t^* = 2000$. This protocol is similar to Ebrahimi et al. (2014).

After this compression and relaxation process, the system is sheared at a constant strain rate using the Lee-Edwards periodic boundary condition. Langevin thermostat is applied with the bias of linear velocity profile during shear. The shear flow is in the X direction, and the Nosé-Hoover barostat is only applied in the Z direction to control the normal stress. The strain rates are given as $\dot{\gamma}^* = 1, 0.4, 0.1, 0.04, 0.01, \text{ and } 0.001$ ($6.93 \times 10^8, 2.77 \times 10^8, 6.93 \times 10^7, 2.77 \times 10^7,$

6.93×10⁶, and 6.93×10⁵ /s) at the normal stresses of P* = 300, 1000, 3000, 6000, and 10000 (1.69, 5.62, 16.85, 33.71, and 56.18 MPa). A reduced time step $\delta t^* = 0.000125$ is used in the case with P = 56.18 MPa and $\dot{\gamma} = 6.93 \times 10^5$ /s. We pay more attention to the system at P = 5.62 MPa, which is comparable to the effective normal stress of 7.0 MPa at the shallow subduction zone that accomodated the large slip in the 2011 Tohoku-Oki earthquake (Ujiie et al., 2013).

To examine the structural change after the flow cessation, the sheared system is hold again and relaxed without shear for the duration of $t^* = 1000$. In this hold period, we adopt two conditions: NVT or NPT. At NVT condition, the system volume is kept constant without the pressure control. At NPT condition, the normal stress in the Z direction is controlled at the same value throughout the shear and the hold. The result is reported in the real unit for comparison with the previous studies.

3 Results

3.1 Porosity and Nematic Order under Compression

Examples of the system configuration are shown in Figure 2. The system is first compressed to reach equilibrium at the given normal stress. The target values are 0.56, 1.69, 5.62, 16.85, 33.71, and 56.18 MPa, respectively. The compaction process is monitored via the porosity (the volume fraction of the pore), which decreases from 0.48 at P = 0.56 MPa to 0.33 at P = 56.18 MPa. (Figure 3a).

The range of porosity in our simulation is similar to some experimental data: e.g. oven-dried Na-Smectite (Likos and Lu, 2006) and partially saturated bentonite at higher normal stress (Baille et al., 2010), whereas Na-Ca-smectite (MX80) saturated with pure water at low normal stress exhibited higher porosity (Marcial et al., 2002).

The difference in porosity may be explained by the ionic conditions of fluid. Our model parameters are determined from the sea water environment, in which the inter-particle space is reduced by the high salt concentration. Since most compression experiments were conducted using pure water, the porosity tends to be higher than that in our simulation.

Porosity also depends on the aspect ratio of clay platelets. A previous MD study shows that platelets with larger aspect ratio (1/25.7 ~ 1/100) tend to gain higher porosity during compression (Ebrahimi et al., 2016). The present study adopts the smaller aspect ratio and therefore relatively lower porosity is realized.

Porosity may also depend on the details of the material and the possible structural change that may occur at larger scale (e.g. micrometers) cannot be captured with the present system size. One should also note that the coarse-grained ellipsoid volume includes the volume of hydrate layers. Taking these points into account, the direct comparison with experiments may not be very fruitful at this stage.

To quantify the orientational order of platelets, the orientational tensor is defined by:

$$Q = \frac{1}{2N} \sum_{i=1}^N (3u_i \otimes u_i - I) \quad (1)$$

where u_i is the unit vector along the symmetry axis of particle i (i.e., the normal vector of platelet i), \otimes denotes the tensor product, I denotes the identity matrix, and N is the total number of ellipsoids in the system. The nematic order parameter S is then defined as the largest

eigenvalue of the orientational tensor Q . When the nematic order parameter vanishes ($S = 0$), the orientation of each platelet is randomly distributed, whereas $S = 1$ means that all the platelets are perfectly aligned. The corresponding eigenvector is referred to as the *director* of the system, which is regarded as the averaged symmetry vector of the platelets. Figure 3b shows that the nematic order increases from 0.37 to 0.47 during compression. Namely, the system becomes more ordered in orientation at higher normal stress. Similar trend is observed in both experimental and simulation studies (Ebrahimi et al., 2016; Perdigon-Aller et al., 2005). Recent meso-scale simulations on clay matrix also suggest less orientational anisotropy for the larger system size (Asadi et al., 2022; Bandera et al., 2021).

3.2 Shear

The stress-strain curves are shown in Figure 4a. Each curve shows a peak and the subsequent weakening with increasing shear strain until reaching a residual strength. The stress peaks around the shear strain of 200% for strain rate below 2.77×10^8 . At higher strain rates, both the peak stress and the steady-state value increase. This trend is in agreement with experiments on crushed and overconsolidated montmorillonite (Haines et al., 2013; Kenigsberg et al., 2019).

Evolution of the volume fraction is shown in Figure 4b. At lower strain rates, the volume fraction increases with strain before reaching the steady-state value. At higher strain rates, the system first dilates then compacts, and the peak of dilation appears during the first 200 % strain. The volume fraction is lower at higher strain rates, but it may take even larger shear strain (larger than 10) to realize the steady state. Comparing the behaviors of shear stress and volume fraction, we find that the maximum of stress coincides with the minimum of volume fraction at higher strain rate.

The nematic order parameter S increases from 0.4 to near 1.0 for all the strain rates, suggesting that the system becomes more orientationally ordered by the shear (Figure 4c). A closer look at a region above $S = 0.9$ (Figure 4d) shows that the nematic order increases quickly to above 0.9 within the shear strain of 200% and then continue to increase slowly until reaching the steady-state value. Systems at higher strain rates reach the similar nematic order above $S = 0.98$, whereas relatively low nematic order is realized at the two lower strain rates (6.93×10^6 and 6.93×10^5 /s).

The shear stress averaged over the strain of 8 to 10 in each run is defined as the steady-state shear stress for further comparison. The result for different strain rates and different normal stresses is summarized in Figure 5a. The shear stress increases with strain rate and normal stress. The shear stress is approximated by the Herschel-Bulkley model:

$$\tau = \tau_0 + K\dot{\gamma}^n \quad (2)$$

Fitting parameters at each normal stress is presented in the supporting information Table S1. The residual value τ_0 denotes the shear stress at zero strain rate limit, which increases with the normal stress (Figure 5b). An approximation with a linear dependence on the normal stress gives the friction coefficient, which turns out to be very small: 0.0135. The residual shear stress at the vanishing normal stress is about 0.25 MPa. The exponent n is below unity in all the cases,

showing the shear-thinning behavior. We find the tendency that the exponent n decreases with normal stress (Figure 5c).

The steady-state friction coefficient is defined by

$$\mu = \tau / \sigma_n \quad (3)$$

The friction coefficient is apparently small and falls in the range of 0.025 to 0.187 as shown in Figure 6a. The friction coefficient decreases with increasing normal stress and increases with strain rate. The volume fraction increases with normal stress and decreases with strain rate (Figure 6b). This is consistent with experiments where dilation is observed in response to the shear velocity increase (Ikari et al., 2009).

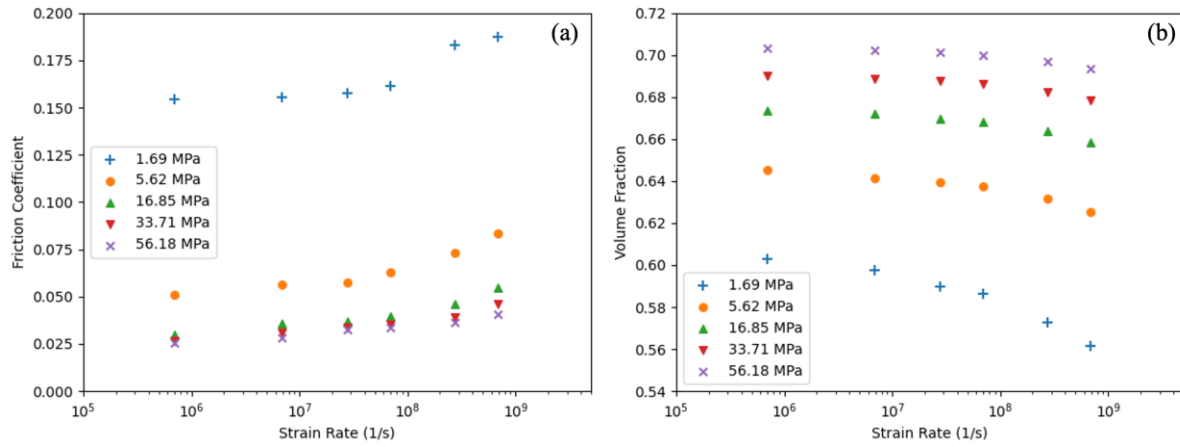


Figure 6. Friction coefficient and volume fraction as a function of strain rate at different normal stresses.

The parallel radial distribution function (PaRDF) is used to characterize the spatial structure of the platelet mixture (Busselez et al., 2014; Caprion et al., 2003; Cienega-Cacerez et al., 2014). The PaRDF is the radial distribution function along the symmetry axis of particle i (i.e., the normal vector of platelet i) $\hat{\mathbf{u}}_i$ and expresses the extent of stacking structure (tactoids formation) of platelets. It is defined as:

$$g^{\parallel}(r) = \frac{V}{N^2 2\pi (\sigma_{ee})^2 h} \left\langle \sum_i \sum_{j \neq i} \delta(r - r_{ij}^{\parallel}) \theta(\sigma_{ee}/2 - |r_{ij}^{\perp}|) \right\rangle \quad (4)$$

where V is the volume of the simulation box, N is the number of ellipsoid particle, h is the cylinder height used to discretize the volume. $r_{ij}^{\parallel} = |\mathbf{r}_{ij}^{\parallel}| = |\mathbf{r}_{ij} \cdot \hat{\mathbf{u}}_i|$ is the center to center distance between particle i and j along the symmetry axis of particle i , and $r_{ij}^{\perp} = |\mathbf{r}_{ij}^{\perp}| = |\mathbf{r}_{ij} - \mathbf{r}_{ij}^{\parallel}|$ is the corresponding perpendicular component. $\theta(x)$ is the Heaviside step function. The sum regarding j is taken only for the particles within the perpendicular distance of the particle radius. For the mixture system, we use the radius of the smallest particle type A (aspect ratio 1/5) for σ_{ee} .

Figure 7a shows the change in PaRDF with the accumulating strain. The initial configuration at zero strain has a short-range correlation with seven pronounced peaks. The peak height decreases with the parallel distance and diminishes to unity around $r = 1.5$. The peak height drops and the peak number decreases during shear: i.e., the decrease in the parallel order. At the shear strain of 10, the peaks have a much lower magnitude and only the first three peaks are recognizable. Namely, the parallel stacking of clay particle is suppressed by the shear.

In each RDF, peaks larger than 1.05 can be fitted with the exponential function:

$$g_{peak} - 1 = A * e^{-r/B} \quad (5)$$

where B defines the characteristic length for parallel stacking. The fitting result for $P = 5.62\text{MPa}$ and $\dot{\gamma} = 6.93 \times 10^8 / \text{s}$ is shown as an example in Figure 7b in semi-log plot. The peaks at zero strain do not strictly follow the exponential line with higher values at larger distance. After the shear is applied, the peaks first drop quickly and reach the lowest curve around the shear strain of 2. Then, in the following 8 strains the peaks increase again gradually but only slightly. Namely, the parallel stacking order does not monotonically declines with the shear strain. However, since the number of appreciable peaks decreases with the shear, the fitting here may not give a sufficient estimation. Fitting parameters are shown in the support information Table S2.

The same analysis is conducted for cases with the strain rate larger than $2.77 \times 10^7 / \text{s}$ at $P = 5.62\text{MPa}$. In Figure 7c, the characteristic stacking size B is shown as a function of shear strain at different strain rates. The result is approximated by an exponential function of the strain:

$$B = C * e^{-\gamma/D} + E \quad (6)$$

where γ is the shear strain, D denotes the characteristic strain, and E denotes the residual value at $\gamma = +\infty$. All the fitting parameters are listed in the support information Table S3. The fitting function (6) generally provides a good estimation, but underestimates the stacking size at the strain of 10 for all strain rate. The steady-state stacking size E decreases with strain rate, this again shows the stacking order is suppressed by the shear (Figure 7c inset).

3.3 Aging at rest

Clay has the complex microscopic structure and exhibits thixotropy. Thixotropy is time-dependent increase of viscosity depending on the shear stress. In a microscopic view, thixotropy is caused by time-dependent restructuring of fabric of the particles in a suspension. Such time-dependent restructuring is referred to as aging. Since thixotropy works as a positive feedback, stick-slip behavior is expected in clay-rich materials (Kameda and Hamada, 2022).

Here we study such time-dependent restructuring in our model clay. Structural analysis using PaRDF is conducted on a system at rest after shear at the normal stress $P = 5.62\text{MPa}$. Shear rate is set to zero after the shear strain of 10 is applied. For the system at rest, we test two different conditions: constant normal stress (NPT) and constant volume (NVT). These two conditions may correspond to drained or undrained conditions at the laboratory scale, respectively. Under the constant volume condition, the system volume remains the same since cessation of shear, while the normal stress is kept fixed under the constant normal stress condition.

The characteristic stacking size B increases during rest, indicating the restoration of the parallel stacking structure during rest (Figure 8). Previous experiments on samples taken from a

phyllosilicate-rich fault observed frictional healing with the hold time, but the healing rate is much smaller than that in phyllosilicate-free materials (Tesei et al., 2012). For clay suspensions and analog yield-stress materials, the logarithmic increase of peak stress with the waiting time is predicted (Bonn et al., 2017). Here we follow these ideas to use the logarithmic function to describe the restoration of stacking size B as a function of the rest time:

$$B = a + b * \log_{10}(t_{rest}) \quad (7)$$

The logarithmic model serves as a reasonable representation of the data for the constant volume condition in Figure 8a, whereas the logarithmic behavior is less apparent for the constant pressure condition in Figure 8b. The fitting parameters are given in the support information Table S4. Figure 8c shows the slope b (the restoration rate of stacking size) as the function of the previous strain rate before rest. Under the constant volume condition, the slope b increases with the previous strain rate. This is because the volume fraction is lower at higher strain rate during shear (Figure 6b). Thus, the particles have more space to reorganize themselves during rest. However, this is true only for the constant volume condition. For the constant pressure condition, pressure control is applied immediately after cessation of shear, and therefore the pore volume is diminished. Accordingly, the slope b is much smaller than that for the constant volume condition, and it increases only slightly with the previous strain rate before rest.

4 Discussion

4.1 Gap between Model Clay and Real Clay Platelets

One of the important features of smectite clay is the large aspect ratio of platelets. The thickness of smectite platelets is typically 1 nm with the layered structure. The length in the diameter direction is often referred to as the size of clay platelets in laboratory investigations. Michot et al. (2004) measured the size distribution of Na-Montmorillonite deduced from the TEM image. The distribution ranges from 5 to 750 nm with the average size of 250 nm. This corresponds to the aspect ratio of 1/5 to 1/750. With regard to the shape, an observation study on individual Na-montmorillonite platelets showed the highly irregular shape (Cadence et al., 2005). The irregular shape and the size polydispersity in the experimental samples may hinder structural ordering or crystallization.

Previous simulation studies on smectite clay often failed to deal with such a large aspect ratio due to the high computational cost. Ebrahimi et al. (2016) used 1,000 particles with the diameters of 25, 42, 60, and 100 nm. Asadi et al. (2022) used 400 particles with the diameters of 6.4 to 19.2 nm. The present study involves a mixture of particles with the diameters of 7.5, 9, and 10.5 nm to facilitate simulation of larger system ($N = 4096$). Clearly, the present study can cover only the smaller particles in the real clay particle size distribution.

The platelet fabric formed in montmorillonite is reported in some previous studies. Clay platelets tend to pile up in the face-to-face direction to form tactoids consisting of 3-8 single platelets (Segad et al., 2012). Larger scale structures of aggregations or gel-like network can be formed in clay suspension at low volume fraction (Michot et al., 2004; Mouzon et al., 2016). Fukukawa et al. (2009) showed that the size of montmorillonite aggregates could increase up to 1200 nm in model sea water. However, in shear experiments at high normal stress and high

volume fraction, large-scale structures or aggregations cannot be clearly identified from SEM images after the shear (Haines et al., 2013; Moore and Lockner, 2007). Presumably, aggregation of platelets may be suppressed by the shear, as confirmed in the present simulation study.

In simulation studies, it is difficult to judge whether a particle belongs to an aggregated cluster. Ebrahimi et al. (2014) applied a strict criterion to analyze aggregated clusters based on the distance and the orientation between platelets. In our study, we adopt the parallel radial distribution, which turns out to be capable of quantifying the nature of stacking structures as well as their time evolution.

The interaction between clay platelets may change drastically depending on the environmental conditions. For instance, when clay platelets are submerged into water, they absorb and exchange cations in the solution, resulting in the negative surface charge. When the salt concentration is high, such as in the sea water environment, the ion-ion correlation force can yield stronger attraction between platelets, allowing particles to aggregate. Water molecules also form layers of crystalline hydrates around a particle. The interaction between two clay platelets thus depends on the complex dynamics of clay, water, and ions. The present study adopts ellipsoid with the Gay-Berne potential, which implements the different interactions for face-to-face and edge-to-edge configurations.

4.2 Shear Resistance

Our model clay system exhibits a velocity strengthening behavior, which is consistent with previous experimental studies on wet smectite (Behnsen and Faulkner, 2013; Brown et al., 2003; Ikari et al., 2007; Moore and Lockner, 2007; Morrow et al., 1992). Similar velocity strengthening behavior is observed by Yamamoto et al. (2005) for disklike particle suspension at low volume fraction. However, the strain rate in this study is much higher than those in typical experiments and natural fault zones.

The shear-rate dependence of shear stress follows the Herschel-Bulkley model with the finite yield stress at the zero strain rate limit. This yield stress increases linearly with the normal stress, with the friction coefficient of 0.0135. Similar linear fitting was reported for natural cation-exchanged montmorillonite, but with the larger friction coefficient of 0.11 to 0.26 (Behnsen and Faulkner, 2013). This discrepancy may be due to the shear resistance of crystalline hydrates, which is not implemented in the present simulation. It may be also due to the larger aspect ratio of natural montmorillonite, which results in stronger attraction force.

The frictional strength of natural montmorillonite is strongly associated with the saturation state (Morrow et al., 2017). For a fully drained and saturated case with the controlled pore pressure, the friction coefficient increases with normal stress (Morrow et al., 1992; Moore and Lockner, 2007; Tembe et al., 2010; Behnsen and Faulkner, 2012; 2013). To the current belief, the friction coefficient increases due to the destruction of crystalline hydrate layers under the high normal stress, reducing the lubrication between clay platelets. In our study, however, the assigned Gay-Berne potential is independent of the shear or the normal stresses, and therefore cannot account for the change in the interlayer hydrate structure or the lubrication effect. Additional features are needed to improve the current model: e.g., the shear resistance of crystalline hydrates and the inter-particle lubrication.

For dry, partially saturated, and over-pressured conditions, the friction coefficient decreases with the normal stress (Saffer and Maroone 2003; Ikari et al., 2007). This normal stress

dependence in dry condition may be linked to the particle alignment (Morrow et al., 2017). At lower pressure, there are more misaligned particles, which tend to rotate by the shear. This results in extra shear resistance. Contrastingly, at higher normal stress, particles tend to be more aligned in the flow direction to reduce the shear resistance.

Previous experimental studies suggest that the formation of fabric and shear bands play a key role in reducing the macroscopic frictional strength in clay-rich gouges (Colletini et al., 2019; Haines et al., 2013; Kenigsberg et al., 2019). However, the nature of fabric structure depends on the aspect ratio of platelets. For this reason, simulation studies with smaller aspect ratio may be incapable of reproducing experimental results that involve fabrics and shear bands. Indeed, shear bands are omnipresent in experiments, but they form only at lower strain rates in the present study. This is discussed in the next subsection.

4.3 Shear Band, Velocity Profile and Particle Orientation

Visual inspection reveals shear banding at lower strain rates, while homogeneous shear occurs at higher strain rates (Figure 2). The velocity profile, the particle orientation profile, and the orientational order are used to determine the phase diagram of sheared system. The velocity profile at $P = 5.62$ MPa is shown in Figure 9a, c. Flow velocity is averaged over every strain increment of 0.5 to get each velocity profile. At strain rate ($\dot{\gamma} = 2.77 \times 10^7$ /s), the velocity profile is relatively linear. At lower strain rate ($\dot{\gamma} = 6.93 \times 10^6$ /s), shear localization is observed.

To characterize the particle orientation, we use the average angle between the symmetry axis of particle and the Z axis. This quantity is shown in Figure 9b, d. They represent the structural rearrangement during shear deformation. The black line at the strain of 0 shows the initial orientation profile. At high strain rate ($\dot{\gamma} = 2.77 \times 10^7$ /s), the velocity profile is linear, and the orientation angle profile becomes homogeneous at large strains. The steady-state value is approximately 10 degrees, indicated by the dashed line. In the presence of shear band ($\dot{\gamma} = 6.93 \times 10^6$ /s), the particle orientation is approximately 10 degrees inside the shear band, whereas it is larger outside the band. Shear banding also explains the low nematic order at lower strain rates shown in Figure 4(d), the overall orientation order is lower than the homogenous cases.

The phase diagram of shear banding is shown in Figure 10. At lower strain rates and/or higher normal stress, shear is accommodated in the shear band. This tendency is common to general yield stress materials (Berthier, 2003).

The structural change can be also probed by the particle orientation. The angle between the Z axis and the symmetry axis of particle is projected on the XZ plane and the YZ plane. These angles are then averaged for all the particles and denoted by θ_{xz} and θ_{yz} , respectively. The evolution of θ_{xz} and θ_{yz} is shown in Figure 11. We find that θ_{xz} approaches 10° at higher strain rate, whereas the angle θ_{yz} approaches 0° . Contrastingly, brownian dynamics simulation with the Gay-Berne potential at low volume fraction (28%) shows that both θ_{xz} and θ_{yz} approach 0° at high strain rate. The difference may be attributed to the low volume fraction, at which the particles rotate and wag (Yamamoto et al., 2005). Recent simulation on spherocylinder suspension shows that the elongated particles tend to align with the flow direction ($\theta_{xz} = 0^\circ$) at low volume fraction (Marschall et al., 2020), while the aligned direction is associated with particle shape at high volume fraction (Börzsönyi et al., 2012; Marschall et al., 2020; Nagy et al.,

2017). Particle alignment was also reported in a shear experiment (Haines et al., 2013), in which the phyllosilicate particles rotate to the orientation perpendicular to the maximum principal stress.

4.4 Structure Development During Shear

In this section, the change in shear stress is compared with the structural change. At lower strain rates, the volume fraction increases quickly in the initial stage of shear (strain 0 to 2) as shown in Figure 4b. The nematic order and the PaRDF also change drastically in this stage (Figures 4c and 7c). Visual inspection (Figure 2) and the velocity profile (Figure 9) suggest that the homogeneous shear is realized for the first 200% strain, and the shear starts to localize afterwards.

In the present study, the initial state has relatively low volume fraction and low orientational order. The system behavior during shear at low strain rates can be classified into two stages. In stage I, the shear stress increases along with the pronounced structural rearrangement in compaction, particle reorientation, and alignment. Parallel stacking structure declines and the shear is relatively homogeneous. These processes occur in the initial stage of shear (strain 0 to 2). Subsequently, in stage II, the system approaches the steady state gradually. The shear stress decreases to the steady-state value with the formation of shear band. The changes in particle orientation and volume fraction is relatively small in stage II.

Kenisberg et al. (2019) hypothesized a micromechanical process of clay-rich gouge under shear along the line of pioneering work such as Logan and Rauenzahn (1987) and Haines et al. (2013). Particle reorientation and compaction occur when the shear strain is relatively small. Fabrics such as Riedel shear, boundary shear, and Y shear start to form after the stress peak and reduce the shear stress. Further weakening with progressive shear is controlled by the development of such fabrics and compaction. The structural change in the present simulation at low strain rates is somewhat consistent with these experimental observations, although the present system may be too small to accommodate various kinds of spatial structures.

5 Conclusions

The rheology and the structure of a simple model for smectite clay are explored by means of coarse-grained molecular dynamics. The particle shape is simplified to oblate ellipsoid, and the Gay-Berne potential is adopted as the simplified interaction. Nevertheless, the present exploratory model is able to capture some important features of a clay system. The system exhibits the velocity-strengthening behavior described by the Herschel-Bulkley law with the exponent smaller than 1. The yield stress in the zero strain rate limit is found to increase linearly with the normal stress. The friction coefficient estimated in this limit is smaller than those in typical experiments. Further improvement of the model, such as the larger particle aspect ratio, crystalline hydrates, and inter-particle lubrication, would enable more quantitative comparison with experiments.

Despite the velocity-strengthening rheology, the present model shows shear banding at lower strain rate and higher normal stress. This may be due to the interplay between the shear and the microstructure of particles (fabric). Inspection on the particle orientation reveals that a specific orientation is preferred in the region where the shear is accommodated. This orientation appears to be controlled by the particle shape rather than the principal stress axes.

506 The structure development at low strain rate is consistent with the hypothesized
507 micromechanical process in some previous experimental studies. Namely, the particles rearrange
508 themselves to align in the shear direction in the first stage (strain of 200%). As a result, the shear
509 stress increases to the maximum value. In the following stage, the shear band starts to form, and
510 the shear stress decreases gradually to the steady-state value.

511 We introduce the PaRDF to probe the change in parallel stacking structure. The
512 characteristic stacking size decreases with the shear strain, and it undergoes logarithmic healing
513 with time in the rest period. The structure restoration rate increases with the previous strain rate
514 before rest. The restoration rate in the constant pressure condition is much smaller than that in
515 the constant volume condition. Namely, healing is more enhanced under the constant volume
516 condition. Although it may give some insights to the healing process in natural fault, one must
517 note that the timescale is very different. More extensive studies are needed to connect this
518 healing behavior in simulation and the healing processes in natural clay-rich faults.

519 Though simple, the present clay model with oblate ellipsoids and the Gay-Berne potential
520 can be still useful to study the rheology and the microstructure of clay systems. However, the
521 present system size may be too small to investigate the effect of larger spatial structures such as
522 Riedel shear. Inspection on larger system is needed to clarify the effects of such spatial
523 structures. Effects of the particle aspect ratio should be also investigated in future to approach the
524 in-situ clay properties. Platelets with larger aspect ratio may have stronger attraction, and thus
525 lead to larger shear resistance and more remarkable structural change by the shear. More
526 understanding on the effects of particle shape may help us generalize the present results to
527 account for a wider class of phyllosilicate minerals.

528

529

530

531

532

533

534

535

536

537

538

539

540

541

542

543

Acknowledgments

This study was supported by JSPS KAKENHI Grant JP21H05201, 22H01145 and JST SPRING Grant JPMJSP2138. Additional support from the MEXT Program: Data Creation and Utilization-Type Material Research and Development Project Grant Number JPMXP1122684766 and “Earthquake and Volcano Hazards Observation and Research Program” are also gratefully acknowledged.

Open Research

Data Availability Statement

The computer codes for LAMMPS simulations of this paper with LAMMPS version information is available through the Zenodo digital repository at: <https://doi.org/10.5281/zenodo.10597892>. Data analysis are carried out using the open-source Python library of NumPy (The NumPy Contributors, 2024; <https://numpy.org>) and Pandas (The Pandas Contributors, 2024; <https://pandas.pydata.org>). Figures are made with the Python library Matplotlib (The Matplotlib Contributors, 2023; <http://www.matplotlib.org/>). Visualization in Figure 2 and part of the data analysis are carried out using the visualization and analysis software OVITO (<https://www.ovito.org>). The Supporting Information contains description of the Gay-Berne potential and fitting parameters used in data analysis.

References

- Aminpour, P., & Sjoblom, K. J. (2019). Multi-scale modelling of kaolinite triaxial behaviour. *Géotechnique Letters*, 9(3), 178-185.
- Asadi, F., Zhu, H. X., Vandamme, M., Roux, J. N., & Brochard, L. (2022). A meso-scale model of clay matrix: the role of hydration transitions in geomechanical behavior. *Soft Matter*, 18(41), 7931-7948.
- Baille, W., Tripathy, S., & Schanz, T. (2010). Swelling pressures and one-dimensional compressibility behaviour of bentonite at large pressures. *Applied Clay Science*, 48(3), 324-333.
- Bandera, S., O'Sullivan, C., Tangney, P., & Angioletti-Uberti, S. (2021). Coarse-grained molecular dynamics simulations of clay compression. *Computers and Geotechnics*, 138, 104333.
- Bayesteh, H., & Hoseini, A. (2021). Effect of mechanical and electro-chemical contacts on the particle orientation of clay minerals during swelling and sedimentation: A DEM simulation. *Computers and Geotechnics*, 130, 103913.
- Behnsen, J., & Faulkner, D. R. (2012). The effect of mineralogy and effective normal stress on frictional strength of sheet silicates. *Journal of Structural Geology*, 42, 49-61.
- Behnsen, J., & Faulkner, D. R. (2013). Permeability and frictional strength of cation-exchanged montmorillonite. *Journal of Geophysical Research: Solid Earth*, 118(6), 2788-2798.
- Berthier, L. (2003). Yield stress, heterogeneities and activated processes in soft glassy materials1. *Journal of Physics: Condensed Matter*, 15(11), S933.
- Bird, P. (1984). Hydration-phase diagrams and friction of montmorillonite under laboratory and geologic conditions, with implications for shale compaction, slope stability, and strength of fault gouge. *Tectonophysics*, 107(3-4), 235-260.

589 Bonn, D., Denn, M. M., Berthier, L., Divoux, T., & Manneville, S. (2017). Yield stress materials
590 in soft condensed matter. *Reviews of Modern Physics*, 89(3), 035005.

591 Börzsönyi, T., Szabó, B., Wegner, S., Harth, K., Török, J., Somfai, E., ... & Stannarius, R.
592 (2012). Shear-induced alignment and dynamics of elongated granular particles. *Physical Review*
593 *E*, 86(5), 051304.

594 Brown, K. M., A. Kopf, M. B. Underwood, and J. L. Weinberger (2003), Compositional and
595 fluid pressure controls on the state of stress on the Nankai subduction thrust: A weak plate
596 boundary, *Earth Planet. Sci. Lett.*, 214, 589–603.

597 Brown, W. M., Petersen, M. K., Plimpton, S. J., & Grest, G. S. (2009). Liquid crystal
598 nanodroplets in solution. *The Journal of chemical physics*, 130(4).

599 Busselez, R., Cerclier, C. V., Ndao, M., Ghoufi, A., Lefort, R., & Morineau, D. (2014). Discotic
600 columnar liquid crystal studied in the bulk and nanoconfined states by molecular dynamics
601 simulation. *The Journal of Chemical Physics*, 141(13).

602 Carpenter, B. M., Marone, C., & Saffer, D. M. (2011). Weakness of the San Andreas Fault
603 revealed by samples from the active fault zone. *Nature Geoscience*, 4(4), 251-254.

604 Caprion, D., Bellier-Castella, L., & Ryckaert, J. P. (2003). Influence of shape and energy
605 anisotropies on the phase diagram of discotic molecules. *Physical Review E*, 67(4), 041703.

606 Chester, F. M., Rowe, C., Ujiie, K., Kirkpatrick, J., Regalla, C., Remitti, F., ... & Expedition 343
607 and 343T Scientists. (2013). Structure and composition of the plate-boundary slip zone for the
608 2011 Tohoku-Oki earthquake. *Science*, 342(6163), 1208-1211.

609 Cienega-Cacerez, O., García-Alcántara, C., Moreno-Razo, J. A., Díaz-Herrera, E., & Sambriski,
610 E. J. (2016). Induced stabilization of columnar phases in binary mixtures of discotic liquid
611 crystals. *Soft Matter*, 12(4), 1295-1312.

Cienega-Cacerez, O., Moreno-Razo, J. A., Díaz-Herrera, E., & Sambriski, E. J. (2014). Phase equilibria, fluid structure, and diffusivity of a discotic liquid crystal. *Soft Matter*, 10(18), 3171-3182.

Colletini, C., Tesei, T., Scuderi, M. M., Carpenter, B. M., & Viti, C. (2019). Beyond Byerlee friction, weak faults and implications for slip behavior. *Earth and Planetary Science Letters*, 519, 245-263.

Coussaert, T., & Baus, M. (2002). Density-functional theory of the columnar phase of discotic Gay–Berne molecules. *The Journal of chemical physics*, 116(17), 7744-7751.

de Bono, J. P., & McDowell, G. R. (2022). Some important aspects of modelling clay platelet interactions using DEM. *Powder Technology*, 398, 117056.

Delhorme, M., Jönsson, B., & Labbez, C. (2014). Gel, glass and nematic states of plate-like particle suspensions: charge anisotropy and size effects. *RSC advances*, 4(66), 34793-34800.

Deng, X., & Underwood, M. B. (2001). Abundance of smectite and the location of a plate-boundary fault, Barbados accretionary prism. *Geological Society of America Bulletin*, 113(4), 495-507.

Dijkstra, M., Hansen, J. P., & Madden, P. A. (1995). Gelation of a clay colloid suspension. *Physical review letters*, 75(11), 2236.

Ebrahimi, D., Whittle, A. J., & Pellenq, R. J. M. (2014). Mesoscale properties of clay aggregates from potential of mean force representation of interactions between nanoplatelets. *The Journal of Chemical Physics*, 140(15).

- Ebrahimi, D., Whittle, A. J., & Pellenq, R. J. M. (2016). Effect of polydispersity of clay platelets on the aggregation and mechanical properties of clay at the mesoscale. *Clays and Clay Minerals*, 64(4), 425-437.
- Furukawa, Y., Watkins, J. L., Kim, J., Curry, K. J., & Bennett, R. H. (2009). Aggregation of montmorillonite and organic matter in aqueous media containing artificial seawater. *Geochemical transactions*, 10, 1-11.
- Gay, J. G., & Berne, B. J. (1981). Modification of the overlap potential to mimic a linear site-site potential. *The Journal of Chemical Physics*, 74(6), 3316-3319.
- Haines, S. H., Kaproth, B., Marone, C., Saffer, D., & Van der Pluijm, B. (2013). Shear zones in clay-rich fault gouge: A laboratory study of fabric development and evolution. *Journal of Structural Geology*, 51, 206-225.
- Ikari, M. J., Saffer, D. M., & Marone, C. (2007). Effect of hydration state on the frictional properties of montmorillonite-based fault gouge. *Journal of Geophysical Research: Solid Earth*, 112(B6).
- Ikari, M. J., Saffer, D. M., & Marone, C. (2009). Frictional and hydrologic properties of clay-rich fault gouge. *Journal of Geophysical Research: Solid Earth*, 114(B5).
- Ikari, M. J., Marone, C., & Saffer, D. M. (2011). On the relation between fault strength and frictional stability. *Geology*, 39(1), 83-86.
- Jeppson, T. N., & Tobin, H. J. (2015). San Andreas fault zone velocity structure at SAFOD at core, log, and seismic scales. *Journal of Geophysical Research: Solid Earth*, 120(7), 4983-4997.
- Kameda, J., Shimizu, M., Ujiie, K., Hirose, T., Ikari, M., Mori, J., ... & Kimura, G. (2015). Pelagic smectite as an important factor in tsunamigenic slip along the Japan Trench. *Geology*, 43(2), 155-158.

656 Kameda, J., & Hamada, Y. (2022). Stick-slip behavior of a clayey crustal fault. *Physical Review*
657 *Research*, 4(1), 013211.

658 Kenigsberg, A. R., Rivière, J., Marone, C., & Saffer, D. M. (2019). The effects of shear strain,
659 fabric, and porosity evolution on elastic and mechanical properties of clay-rich fault gouge.
660 *Journal of Geophysical Research: Solid Earth*, 124, 10,968–10,982.

661 Kenigsberg, A. R., Rivière, J., Marone, C., & Saffer, D. M. (2020). Evolution of elastic and
662 mechanical properties during fault shear: The roles of clay content, fabric development, and
663 porosity. *Journal of Geophysical Research: Solid Earth*, 125(3), e2019JB018612.

664 Kutter, S., Hansen, J. P., Sprik, M., & Boek, E. (2000). Structure and phase behavior of a model
665 clay dispersion: A molecular-dynamics investigation. *The Journal of Chemical Physics*, 112(1),
666 311-322.

667 Likos, W. J., & Lu, N. (2006). Pore-scale analysis of bulk volume change from crystalline
668 interlayer swelling in Na⁺- and Ca²⁺-smectite. *Clays and Clay Minerals*, 54(4), 515-528.

669 Lockner, D. A., Morrow, C., Moore, D., & Hickman, S. (2011). Low strength of deep San
670 Andreas fault gouge from SAFOD core. *Nature*, 472(7341), 82-85.

671 Luckhurst, G. R., & Simmonds, P. S. J. (1993). Computer simulation studies of anisotropic
672 systems: XXI. Parametrization of the Gay-Berne potential for model mesogens. *Molecular*
673 *Physics*, 80(2), 233-252.

674 Marcial, D., Delage, P., & Cui, Y. J. (2002). On the high stress compression of bentonites.
675 *Canadian Geotechnical Journal*, 39(4), 812-820.

676 Marschall, T. A., Van Hoesen, D., & Teitel, S. (2020). Shear-driven flow of athermal,
677 frictionless, spherocylinder suspensions in two dimensions: Particle rotations and orientational
678 ordering. *Physical Review E*, 101(3), 032901.

Michot, L. J., Bihannic, I., Porsch, K., Maddi, S., Baravian, C., Mougél, J., & Levitz, P. (2004). Phase diagrams of Wyoming Na-montmorillonite clay. Influence of particle anisotropy. *Langmuir*, 20(25), 10829-10837.

Moore, D. E., & Lockner, D. A. (2007). Friction of the smectite clay montmorillonite: A review and interpretation of data. *The seismogenic zone of subduction thrust faults*, 317-345.

Morrow, C., B. Radney, and J. Byerlee (1992), Frictional strength and the effective pressure law of montmorillonite and illite clays, in *Fault Mechanisms and Transport Properties of Rocks*, edited by B. Evans and T.-F. Wong, pp. 69–88, Elsevier, New York.

Morrow, C. A., Moore, D. E., & Lockner, D. A. (2017). Frictional strength of wet and dry montmorillonite. *Journal of Geophysical Research: Solid Earth*, 122(5), 3392-3409.

Mouzon, J., Bhuiyan, I. U., & Hedlund, J. (2016). The structure of montmorillonite gels revealed by sequential cryo-XHR-SEM imaging. *Journal of Colloid and Interface Science*, 465, 58-66.

Nagy, D. B., Claudin, P., Börzsönyi, T., & Somfai, E. (2017). Rheology of dense granular flows for elongated particles. *Physical Review E*, 96(6), 062903.

Niemeijer, A., Marone, C., & Elsworth, D. (2010). Fabric induced weakness of tectonic faults. *Geophysical Research Letters*, 37(3).

Odriozola, G., Romero-Bastida, M., & Guevara-Rodriguez, F. D. J. (2004). Brownian dynamics simulations of Laponite colloid suspensions. *Physical Review E*, 70(2), 021405.

Pagano, A. G., Magnanimo, V., Weinhart, T., & Tarantino, A. (2020). Exploring the micromechanics of non-active clays by way of virtual DEM experiments. *Géotechnique*, 70(4), 303-316.

Paineau, E., Philippe, A. M., Antonova, K., Bihannic, I., Davidson, P., Dozov, I., ... & Michot, L. J. (2013). Liquid–crystalline properties of aqueous suspensions of natural clay nanosheets. *Liquid Crystals Reviews*, 1(2), 110-126.

Pellenq, R. M., Caillol, J. M., & Delville, A. (1997). Electrostatic attraction between two charged surfaces: A (N, V, T) Monte Carlo simulation. *The Journal of Physical Chemistry B*, 101(42), 8584-8594.

Perdigon-Aller, A. C., Aston, M., & Clarke, S. M. (2005). Preferred orientation in filtercakes of kaolinite. *Journal of colloid and interface science*, 290(1), 155-165.

Ruzicka, B., Zaccarelli, E., Zulian, L., Angelini, R., Sztucki, M., Moussaïd, A., ... & Sciortino, F. (2011). Observation of empty liquids and equilibrium gels in a colloidal clay. *Nature materials*, 10(1), 56-60.

Saffer, D. M., & Marone, C. (2003). Comparison of smectite-and illite-rich gouge frictional properties: application to the updip limit of the seismogenic zone along subduction megathrusts. *Earth and Planetary Science Letters*, 215(1-2), 219-235.

Segad, M., Jönsson, B., & Cabane, B. (2012). Tactoid formation in montmorillonite. *The Journal of Physical Chemistry C*, 116(48), 25425-25433.

Shen, X., & Bourg, I. C. (2021). Molecular dynamics simulations of the colloidal interaction between smectite clay nanoparticles in liquid water. *Journal of Colloid and Interface Science*, 584, 610-621.

Stukowski, A. (2009). Visualization and analysis of atomistic simulation data with OVITO—the Open Visualization Tool. *Modelling and simulation in materials science and engineering*, 18(1), 015012.

- Summers, R., & Byerlee, J. (1977, May). A note on the effect of fault gouge composition on the stability of frictional sliding. In *International Journal of Rock Mechanics and Mining Sciences & Geomechanics Abstracts* (Vol. 14, No. 3, pp. 155-160). Pergamon.
- Tembe, S., Lockner, D. A., & Wong, T. F. (2010). Effect of clay content and mineralogy on frictional sliding behavior of simulated gouges: Binary and ternary mixtures of quartz, illite, and montmorillonite. *Journal of Geophysical Research: Solid Earth*, 115(B3).
- Tesei, T., Collettini, C., Carpenter, B. M., Viti, C., & Marone, C. (2012). Frictional strength and healing behavior of phyllosilicate-rich faults. *Journal of Geophysical Research: Solid Earth*, 117(B9).
- The NumPy Contributors. (2024). NumPy: Fundamental package for array computing in Python [Software]. Retrieved from <https://pypi.org/project/numpy/>
- The Matplotlib Contributors. (2023). Matplotlib: Python plotting package in Python [Software]. Retrieved from <https://pypi.org/project/matplotlib/>
- The Pandas Contributors. (2024). Pandas: Powerful data structures for data analysis, time series, and statistics in Python [Software]. Retrieved from <https://pypi.org/project/pandas/>
- Thompson, A. P., Aktulga, H. M., Berger, R., Bolintineanu, D. S., Brown, W. M., Crozier, P. S., ... & Plimpton, S. J. (2022). LAMMPS-a flexible simulation tool for particle-based materials modeling at the atomic, meso, and continuum scales. *Computer Physics Communications*, 271, 108171.
- Thuresson, A., Jansson, M., Plivelic, T. S., & Skepö, M. (2017). Temperature response of charged colloidal particles by mixing counterions utilizing Ca²⁺/Na⁺ montmorillonite as model system. *The Journal of Physical Chemistry C*, 121(14), 7951-7958.

Ujiie, K., Tanaka, H., Saito, T., Tsutsumi, A., Mori, J. J., Kameda, J., ... & Expedition 343 and
 343T Scientists. (2013). Low coseismic shear stress on the Tohoku-Oki megathrust determined
 from laboratory experiments. *Science*, 342(6163), 1211-1214.

Underwood, T. R., & Bourg, I. C. (2020). Large-scale molecular dynamics simulation of the
 dehydration of a suspension of smectite clay nanoparticles. *The Journal of Physical Chemistry C*,
 124(6), 3702-3714.

Wojatschke, J., Scuderi, M. M., Warr, L. N., Carpenter, B. M., Saffer, D., & Marone, C. (2016).
 Experimental constraints on the relationship between clay abundance, clay fabric, and frictional
 behavior for the Central Deforming Zone of the San Andreas Fault. *Geochemistry,
 Geophysics, Geosystems*, 17(10), 3865-3881.

Wu, F. T., Blatter, L., & Roberson, H. (1975). Clay gouges in the San Andreas fault system and
 their possible implications. *Earthquake Prediction and Rock Mechanics*, 87-95.

Yamamoto, T., Suga, T., & Mori, N. (2005). Brownian dynamics simulation of orientational
 behavior, flow-induced structure, and rheological properties of a suspension of oblate spheroid
 particles under simple shear. *Physical Review E*, 72(2), 021509.

Figure 1. The (dimensionless) Gay-Berne potential vs the (dimensionless) distance for two
 typical configurations of ellipsoid particles. Three particle types (A, B, and C) correspond to the
 aspect ratio of 1/5, 1/6 and 1/7, respectively. Solid lines represent the potential for face-to-face
 configuration, labeled with “f-f” in the legend. Similarly, dashed lines represent potential for
 edge-to-edge configuration, labeled with “e-e”. The energy ratio between the two configurations
 (“e-e” and “f-f”) is 1/5 for all the particles.

Figure 2. Examples of compression and shear configurations at normal stress $P = 5.62\text{MPa}$, a
 view on the XZ plane. (a) Compressed system colored by different particle aspect ratio, where
 red, blue, and yellow correspond to particle aspect ratio of 1/5, 1/6, and 1/7. (b) Mixture system
 colored by the x coordinate of particles at strain of 0, the same coloring is used for (b), (c), and
 (d). Two scenarios are observed with (c) the homogeneous shear at high strain rate $2.77 \times 10^7 / \text{s}$
 and (d) the shear band at low strain rate $6.93 \times 10^6 / \text{s}$.

Figure 3. Porosity and nematic order as a function of normal stress during compression. Solid circle: present study, compressed to the normal stress of 0.56, 1.69, 5.62, 16.85, 33.71, and 56.18 MPa. Hollow circle: saturated Na-Ca-smectite (Marcial et al., 2002). Plus: oven-dried Na-smectite (Likos and Lu, 2006). Cross: partially saturated bentonite (Baille et al., 2010).

Figure 4. Example of (a) shear stress, (b) volume fraction, and (c, d) nematic order parameter as a function of shear strain for all strain rates at the normal stress of 5.62 MPa. Dashed line is a guide line of the position of peak shear stress around the strain of 200% for lower strain rate cases. The two highest strain rates experienced the peak stress at early strain, close to the position of dilation in volume fraction. (d) A zoom at larger nematic order shows the two lowest strain rates reached slightly lower order.

Figure 5. (a) Shear stress as a function of strain rate at different normal stresses, fitted with Herschel-Bulkley model. (b) The residual shear stress at zero strain rate limit increases with normal stress. The dotted line is the approximation with a linear model. (c) The exponent decrease with normal stress. The dotted line is the approximation with a linear model.

Figure 6. Friction coefficient and volume fraction as a function of strain rate at different normal stresses.

Figure 7. Change in the parallel stacking structure during shear. (a) The parallel stacking structure is first probed with PaRDF for the system at $P = 5.62$ MPa and $\dot{\gamma} = 6.93 \times 10^8$ /s. Each curve represents a PaRDF at a certain strain. The peak height and the peak number decrease with shear strain. (b) The peak value as a function of distance is fitted with an exponential function from equation (5). (c) A characteristic stacking size B is determined from the change in PaRDF and decreases to a residual value during shear following equation (6). The inset shows the steady-state stacking size E decreases with strain rate.

Figure 8. The characteristic stacking size increases with the rest time under (a) the constant volume condition and (b) the constant normal stress condition. The lines represent the logarithmic equation (7). (c) The slope b , the restoration rate of the stacking size, increases with the strain rate before the rest.

Figure 9. Inspection on shear banding from velocity profile and particle orientation profile. The flow is homogeneous at high strain rate (a), whereas shear band is formed at low strain rate (c). Profile of the average angle between the symmetry axis of platelet and the Z axis. The black line represents the initial structure. The flow becomes homogeneous at high strain rate (b) while the particle orientation approaches 10 degrees inside the shear band at low strain rate (d).

Figure 10. The phase diagram of shear band in the range of normal stress and strain rate investigated. Shear band is more likely to occur at lower strain rate and higher normal stress.

Figure 11. Example of angle between the director and the Z-axis as a function of shear strain for all strain rates at the normal stress of 5.62 MPa. (a) The angle between the director and the Z-axis approaches 10° in the XZ plane and (b) approaches 0° in the YZ plane at high strain rate.

Figure 1.

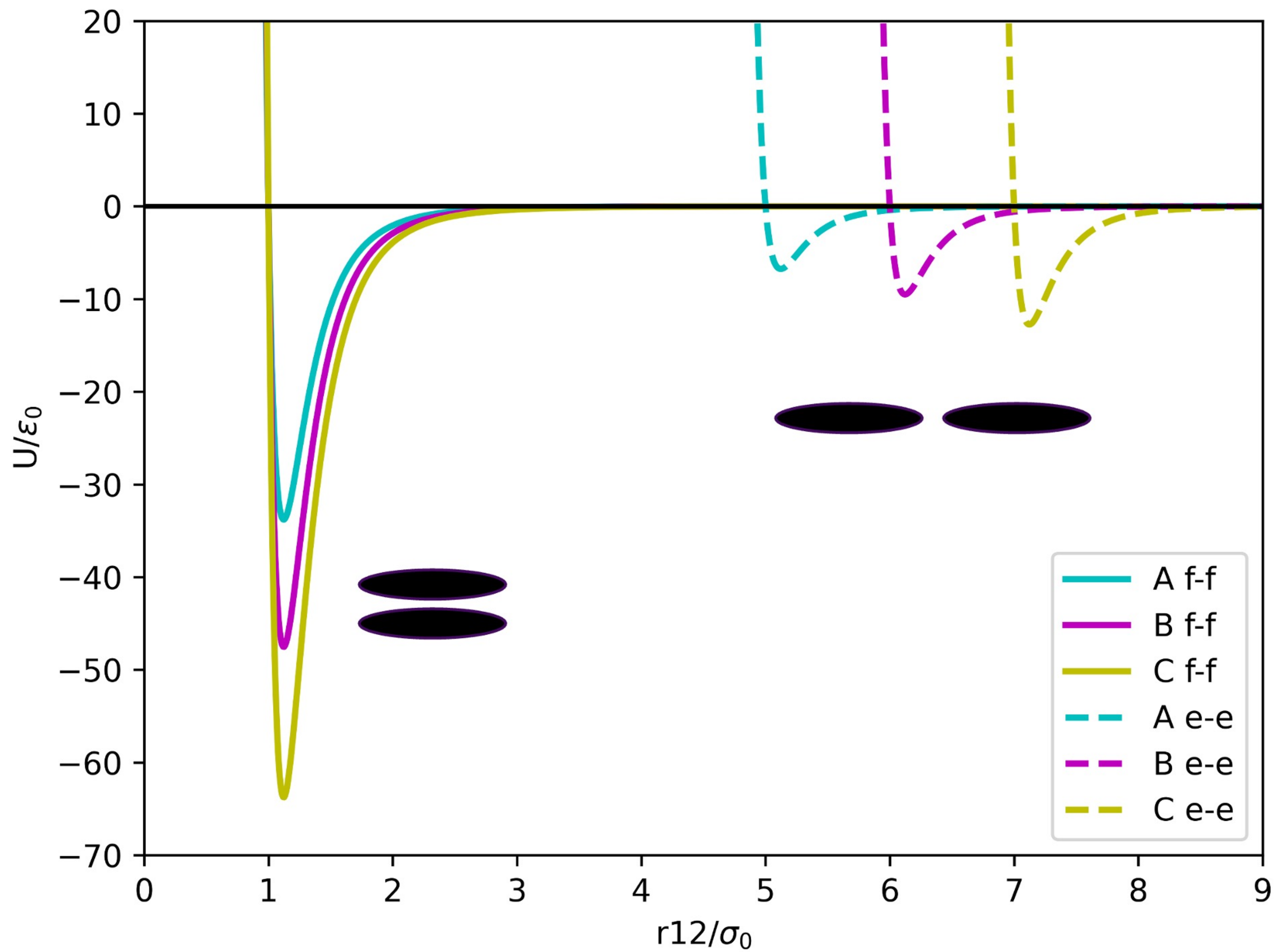
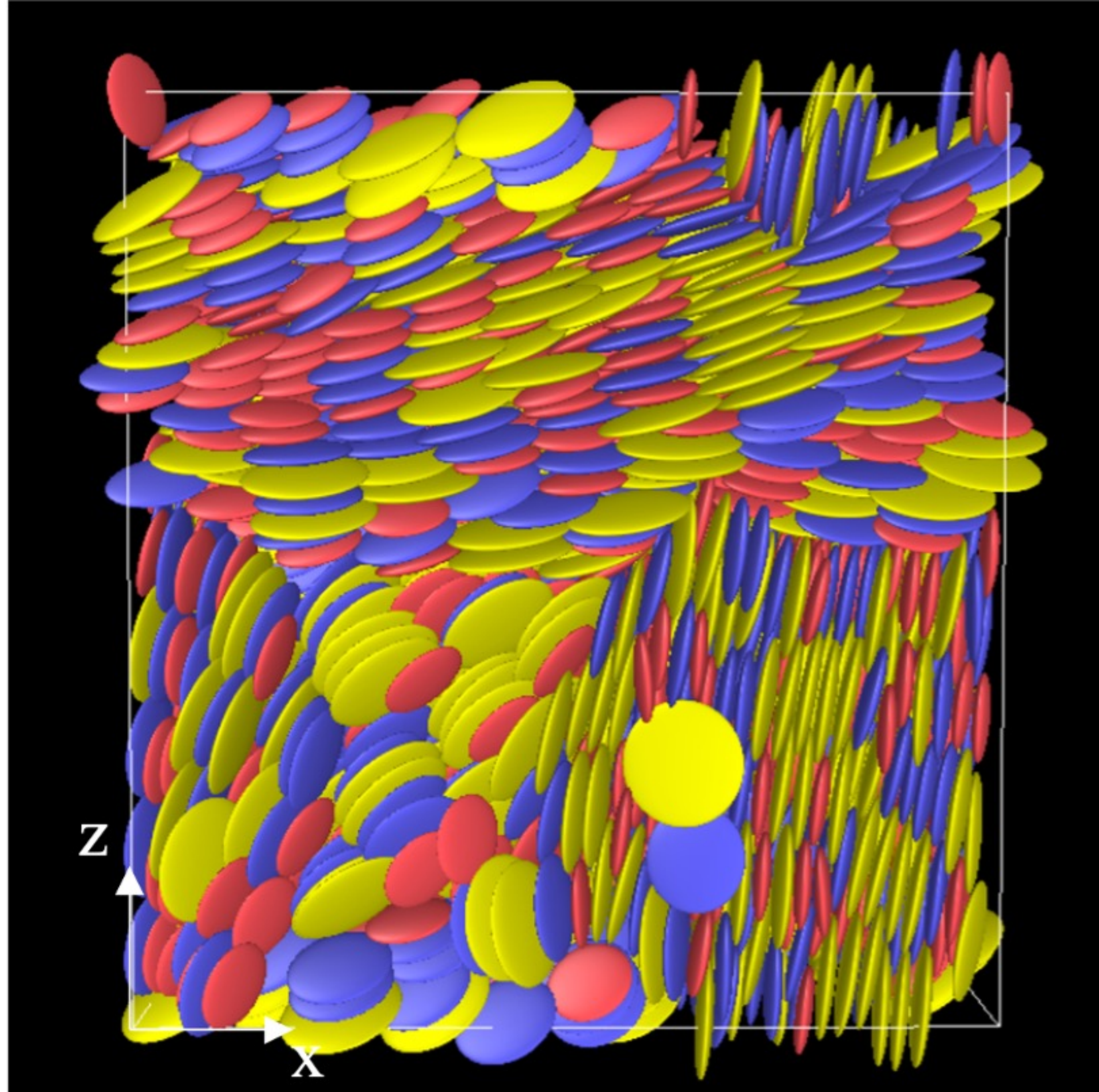
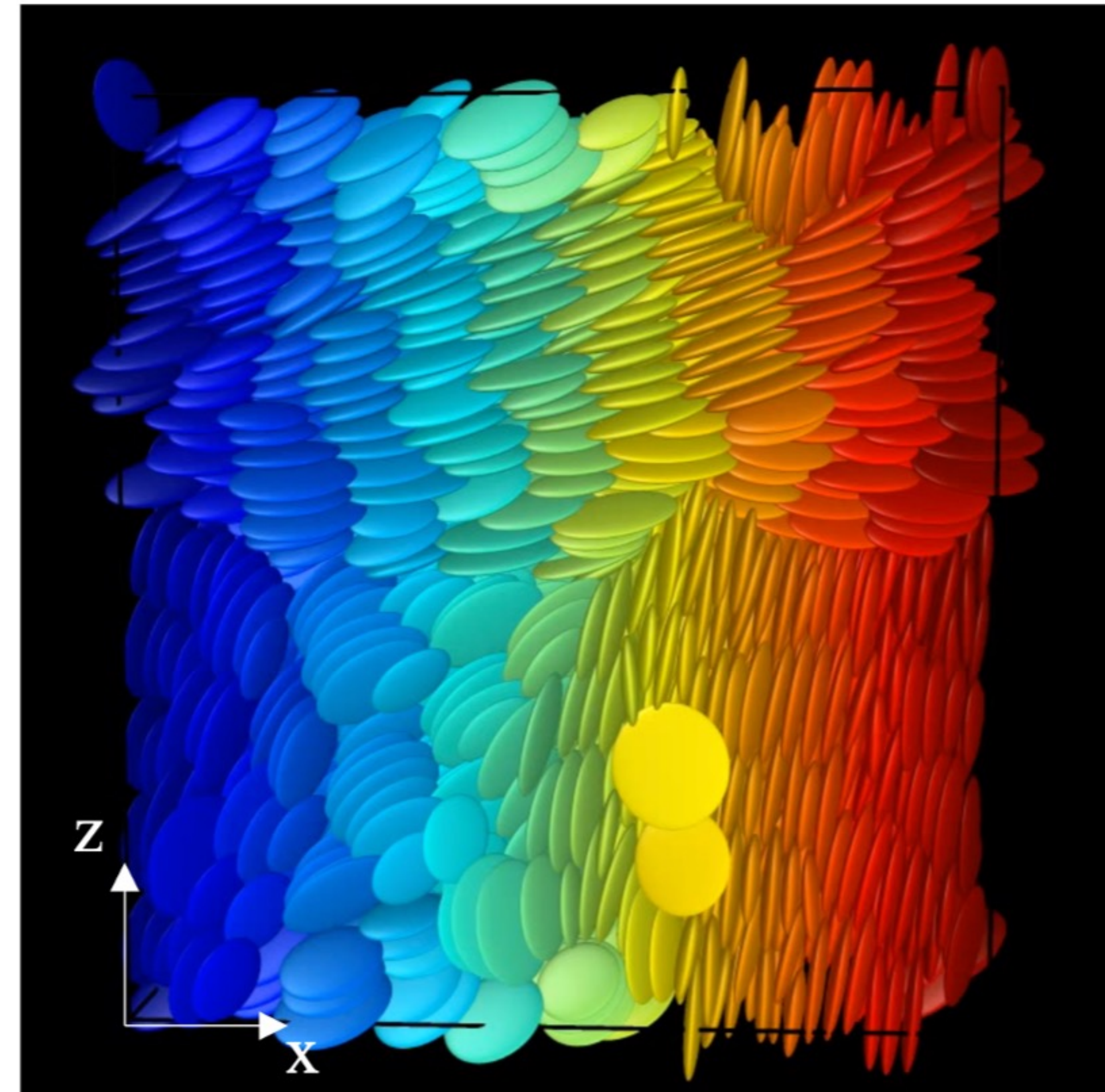


Figure 2.



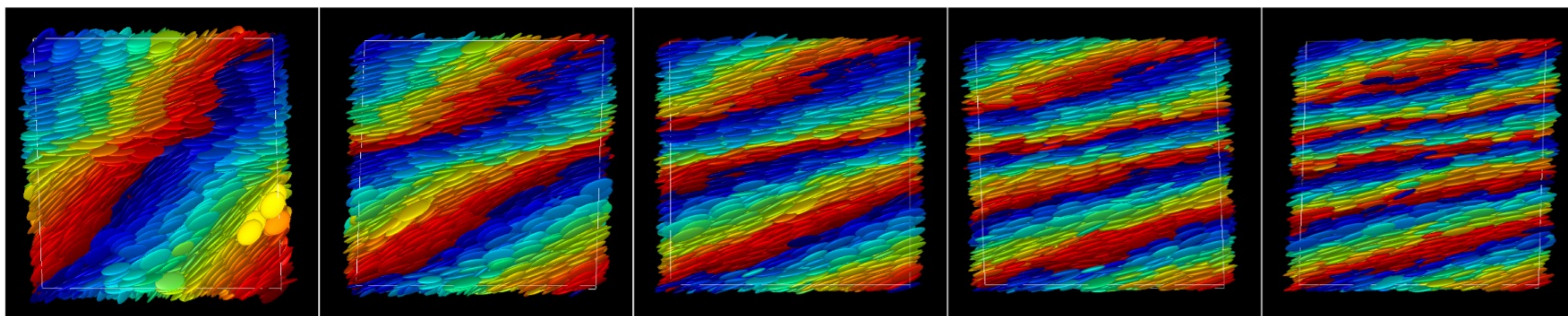
(a)



(b)

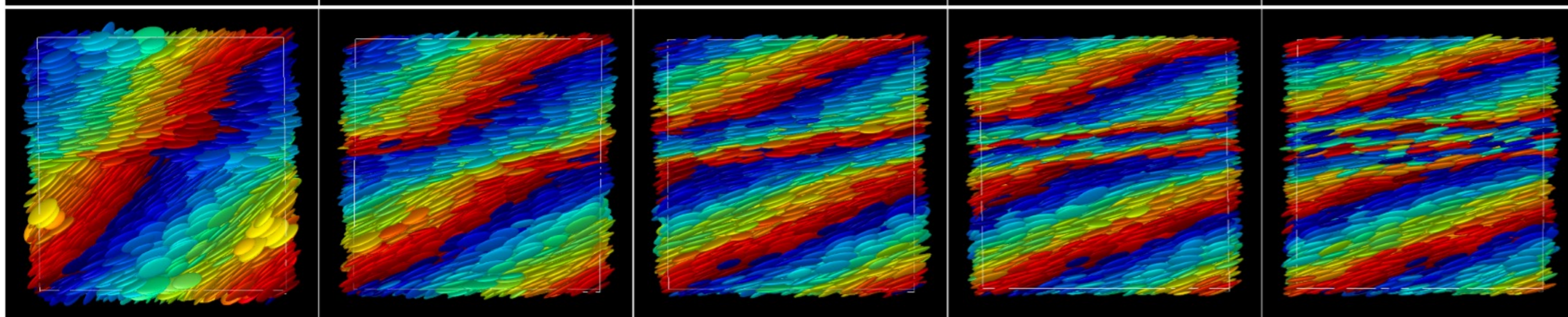
(c)

$\dot{\gamma}=2.77 \times 10^7$ /s
Homogeneous



(d)

$\dot{\gamma}=6.93 \times 10^6$ /s
Shear band



~1 strain

~2 strain

~3 strain

~4 strain

~5 strain

Figure 3.

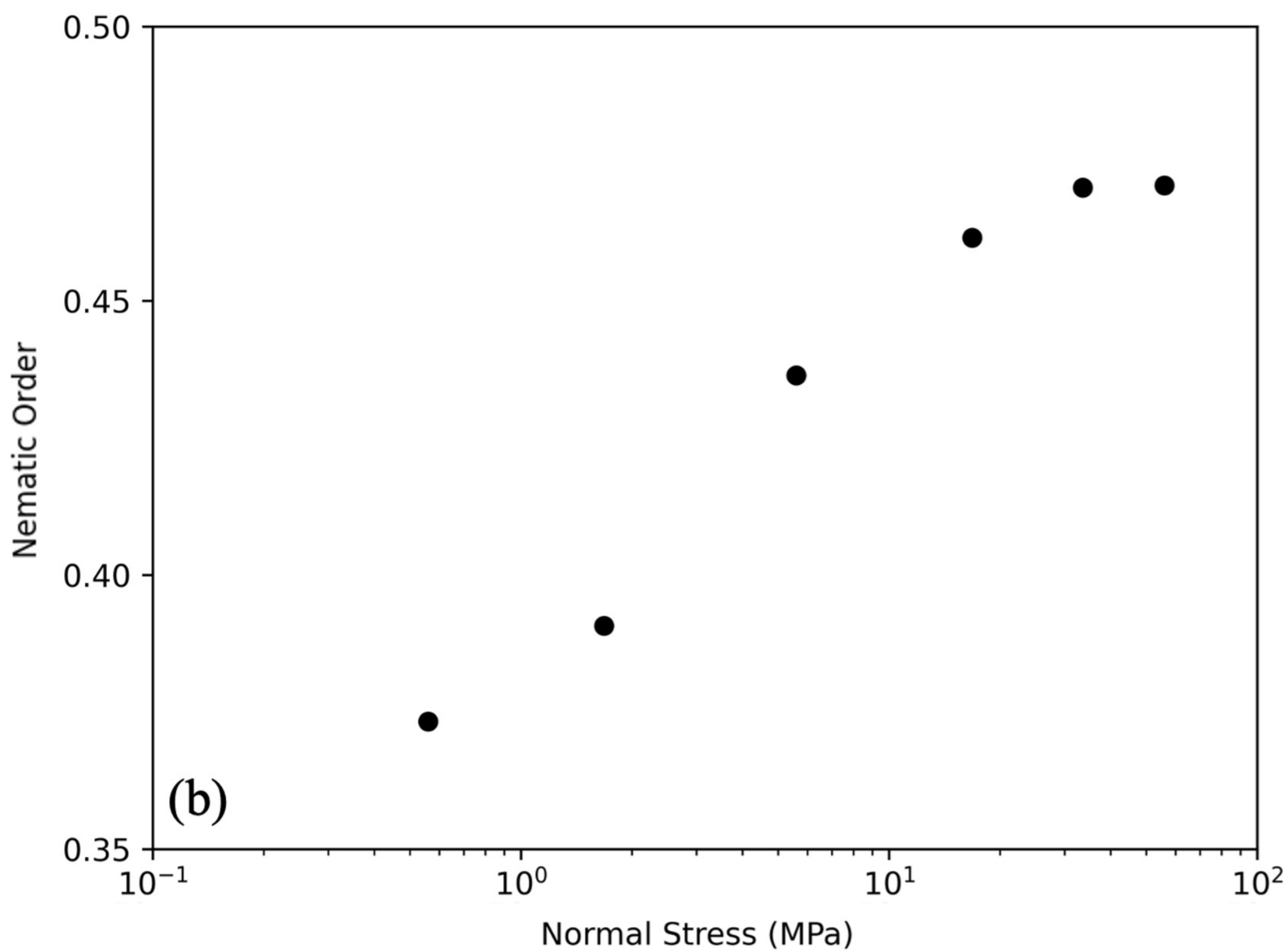
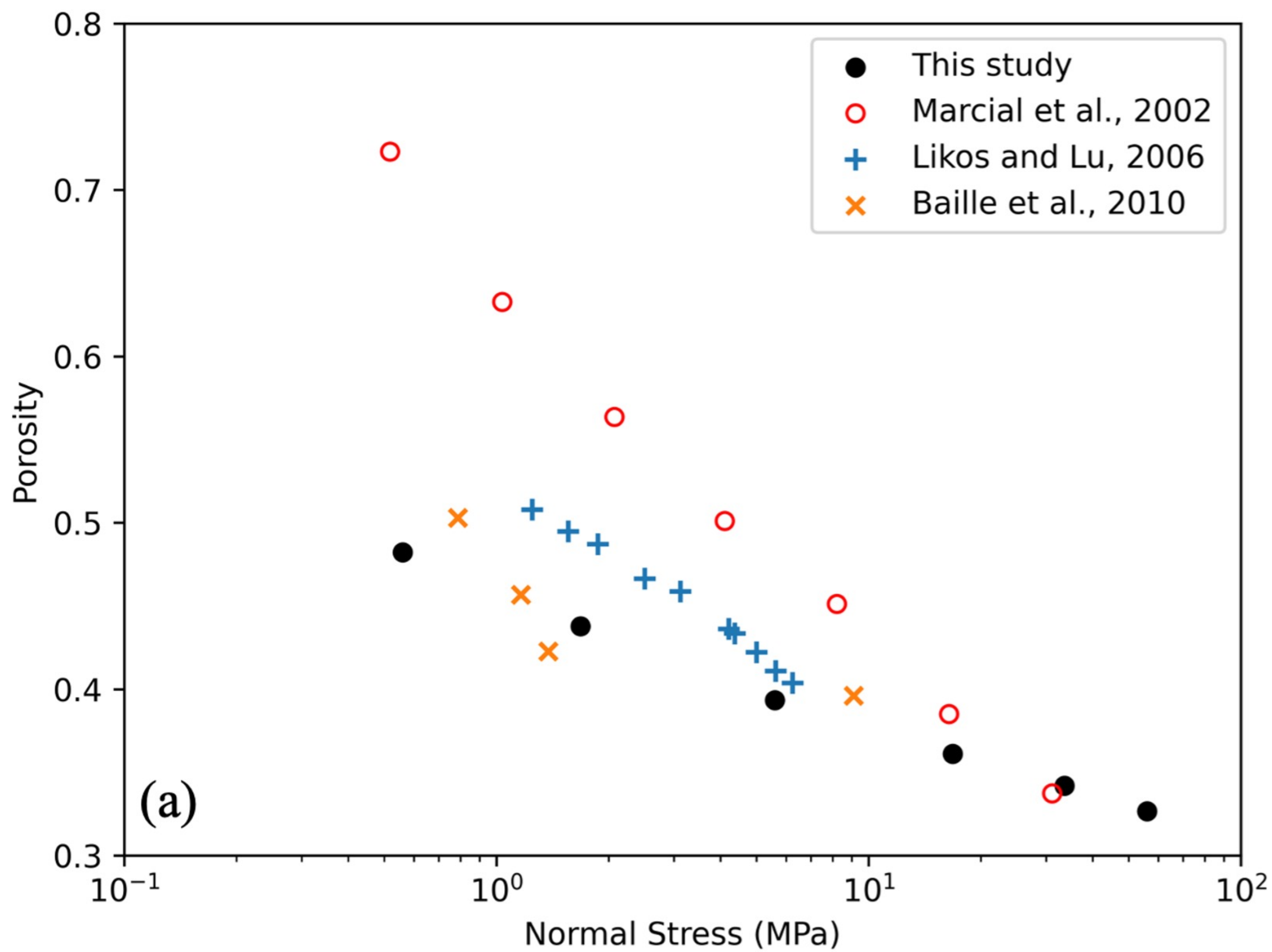


Figure 4.

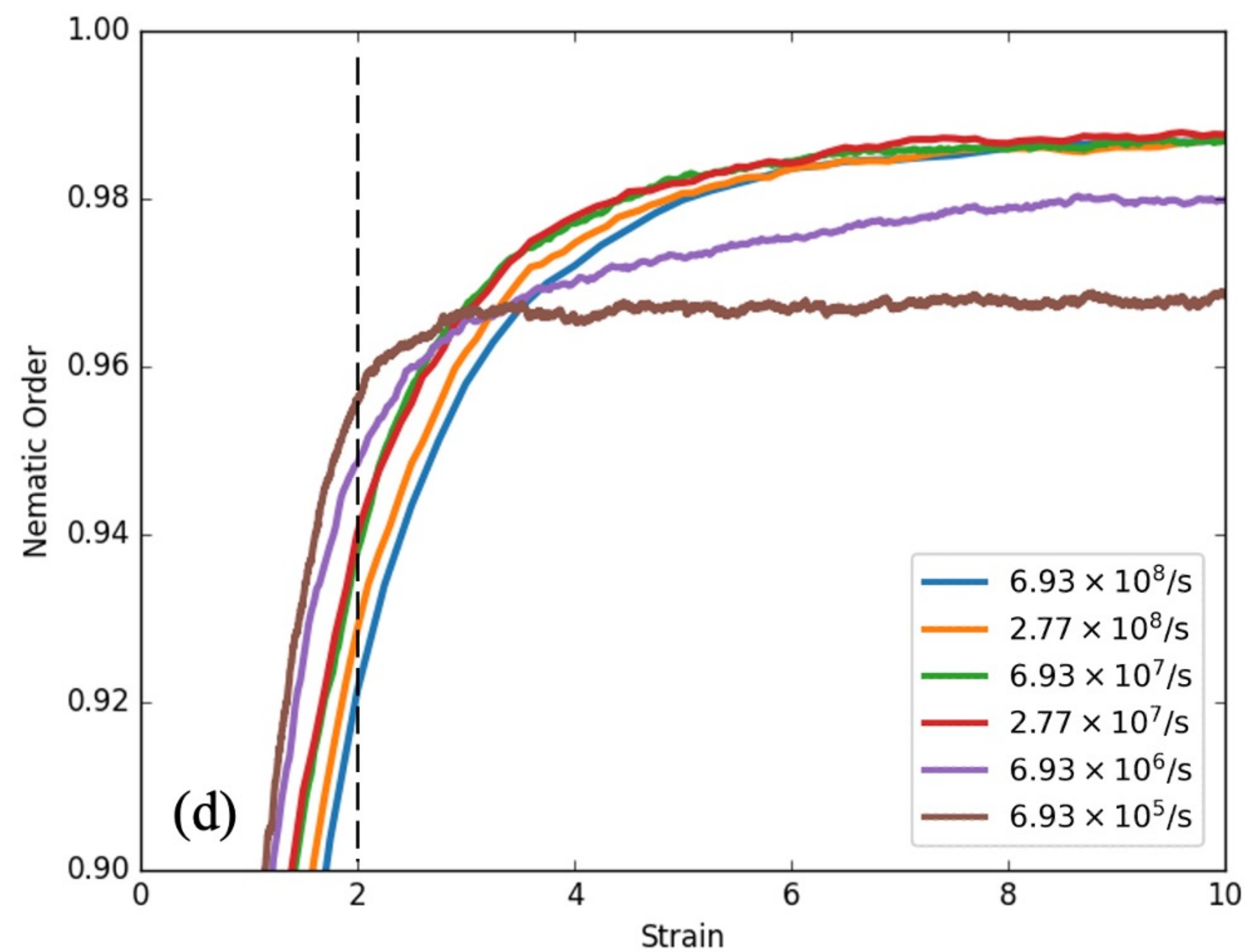
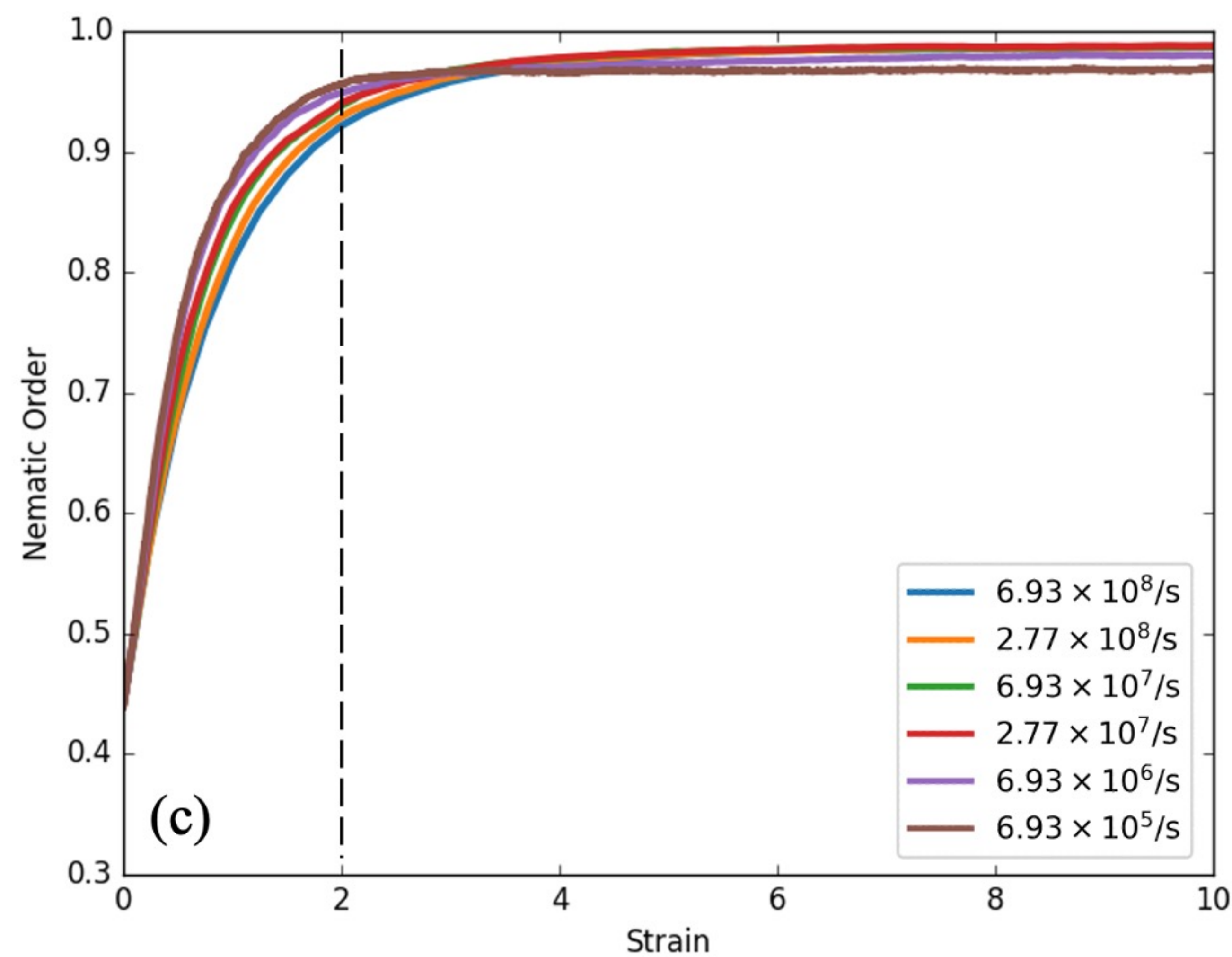
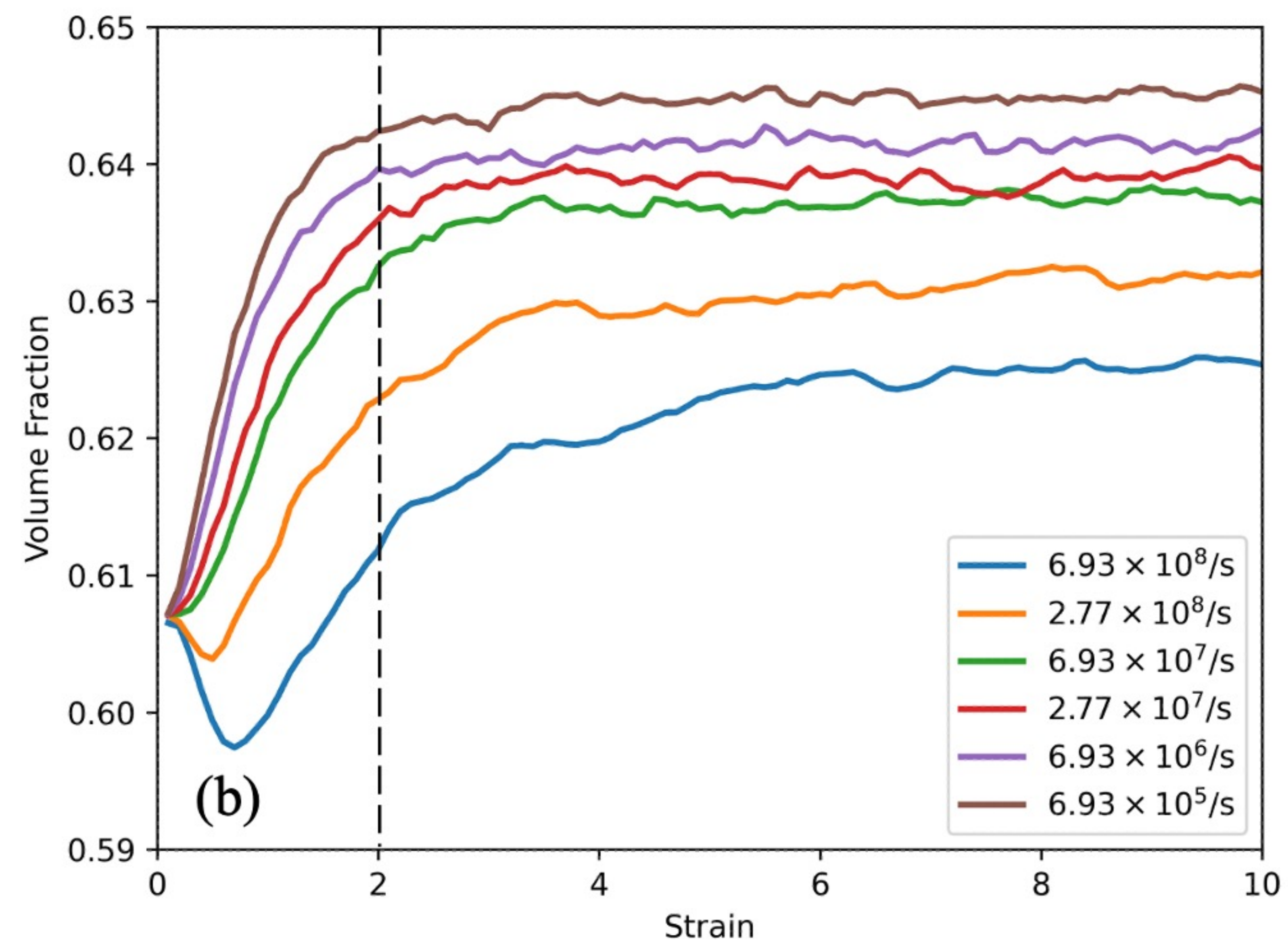
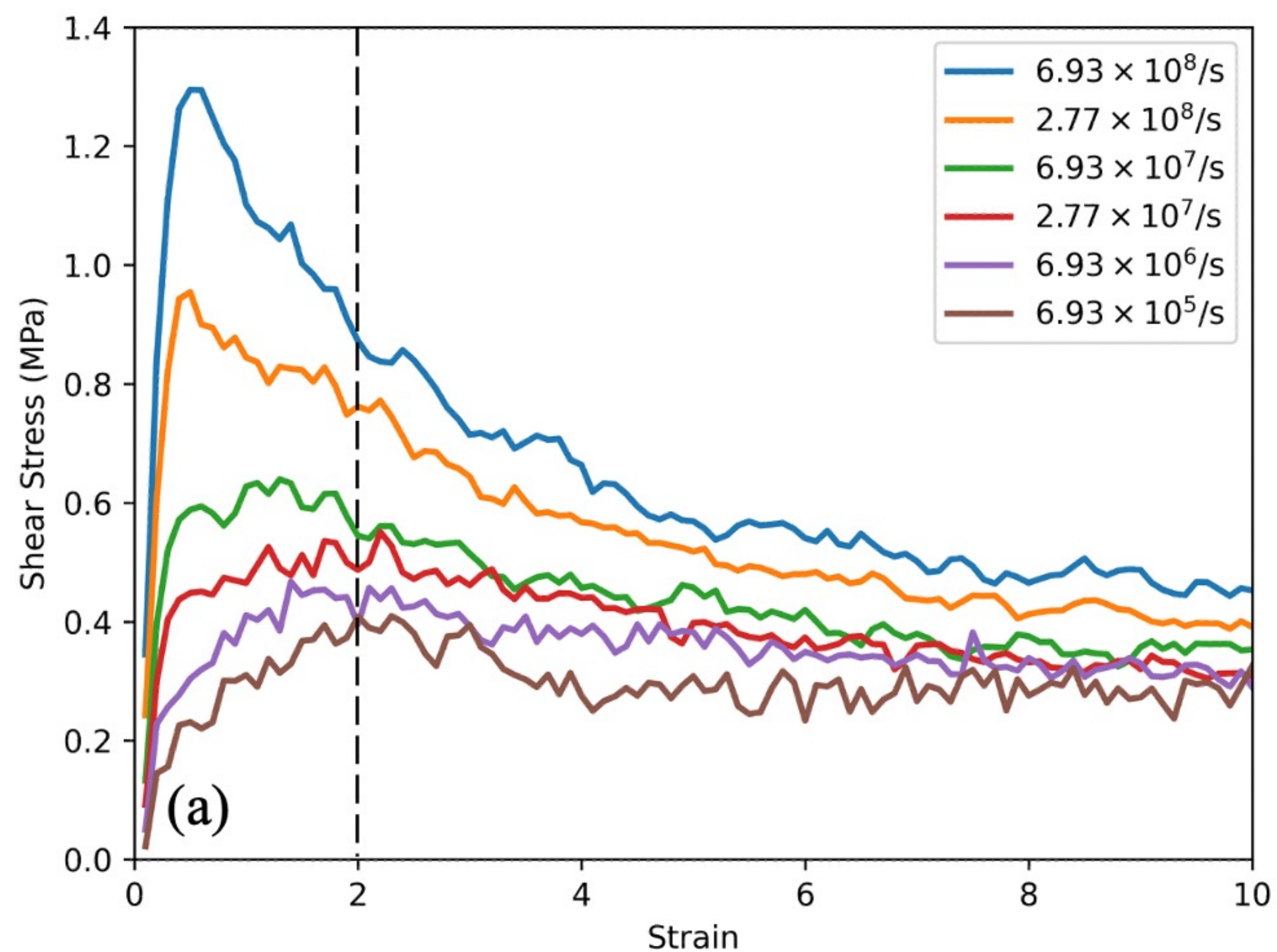


Figure 5.

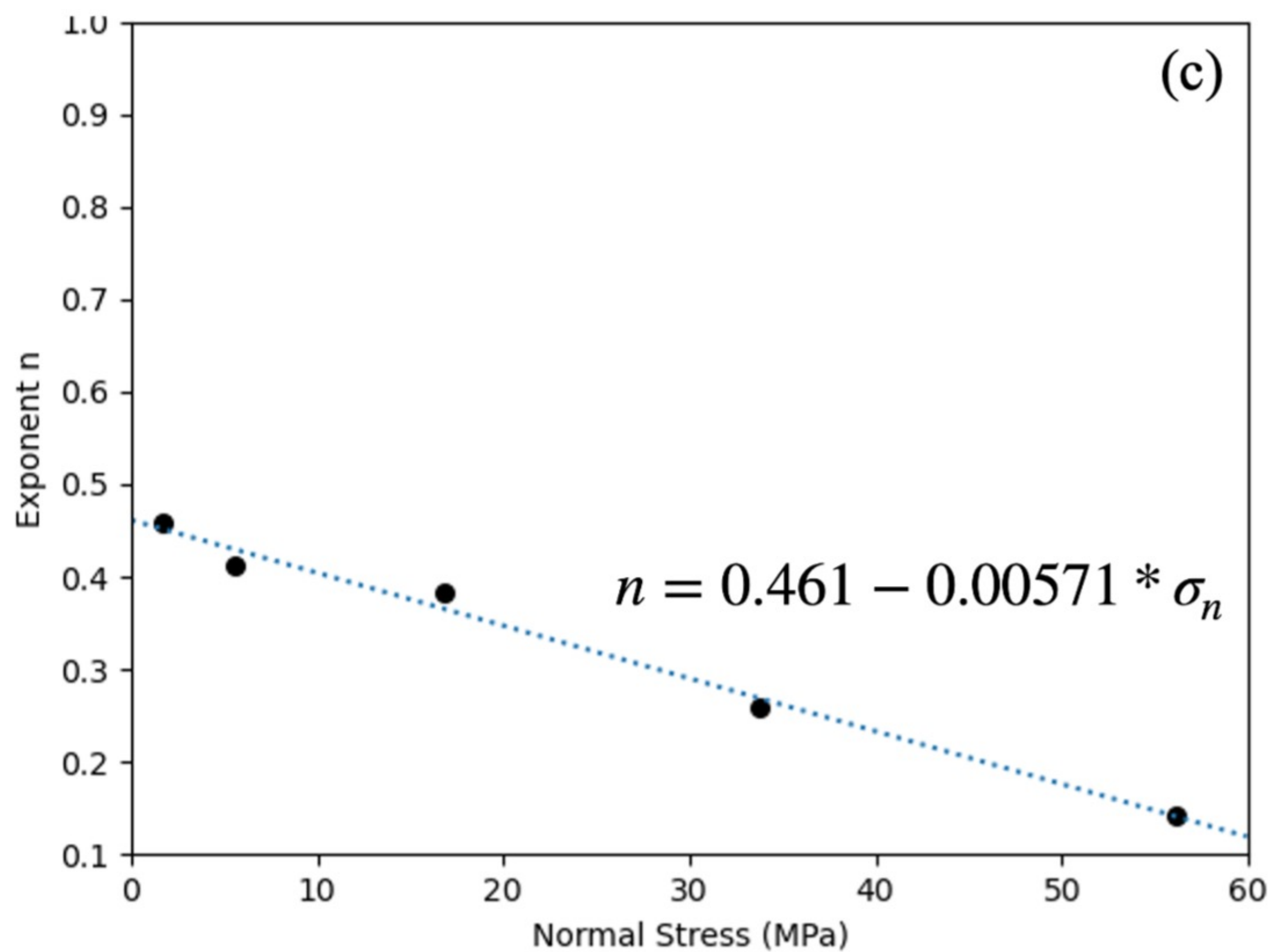
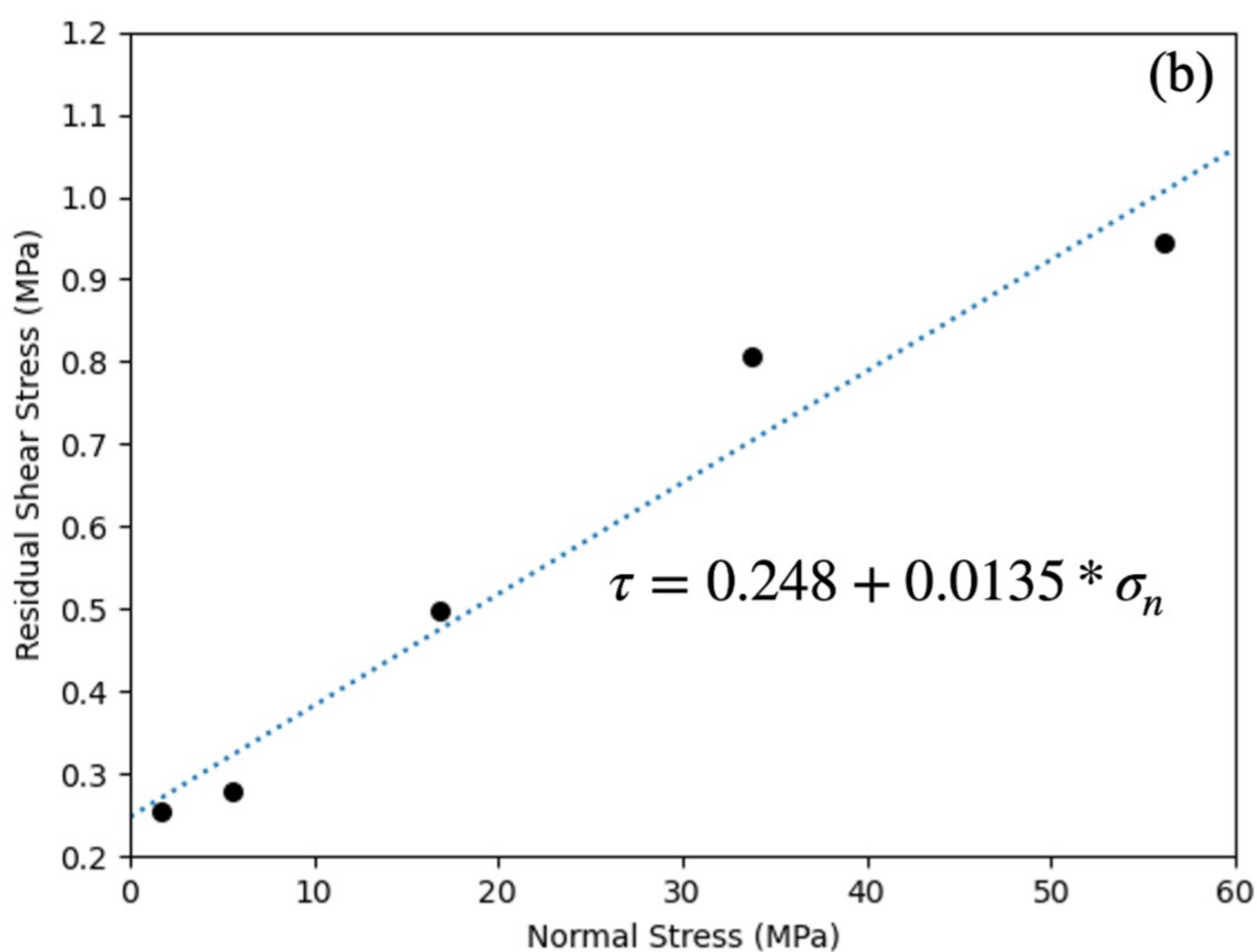
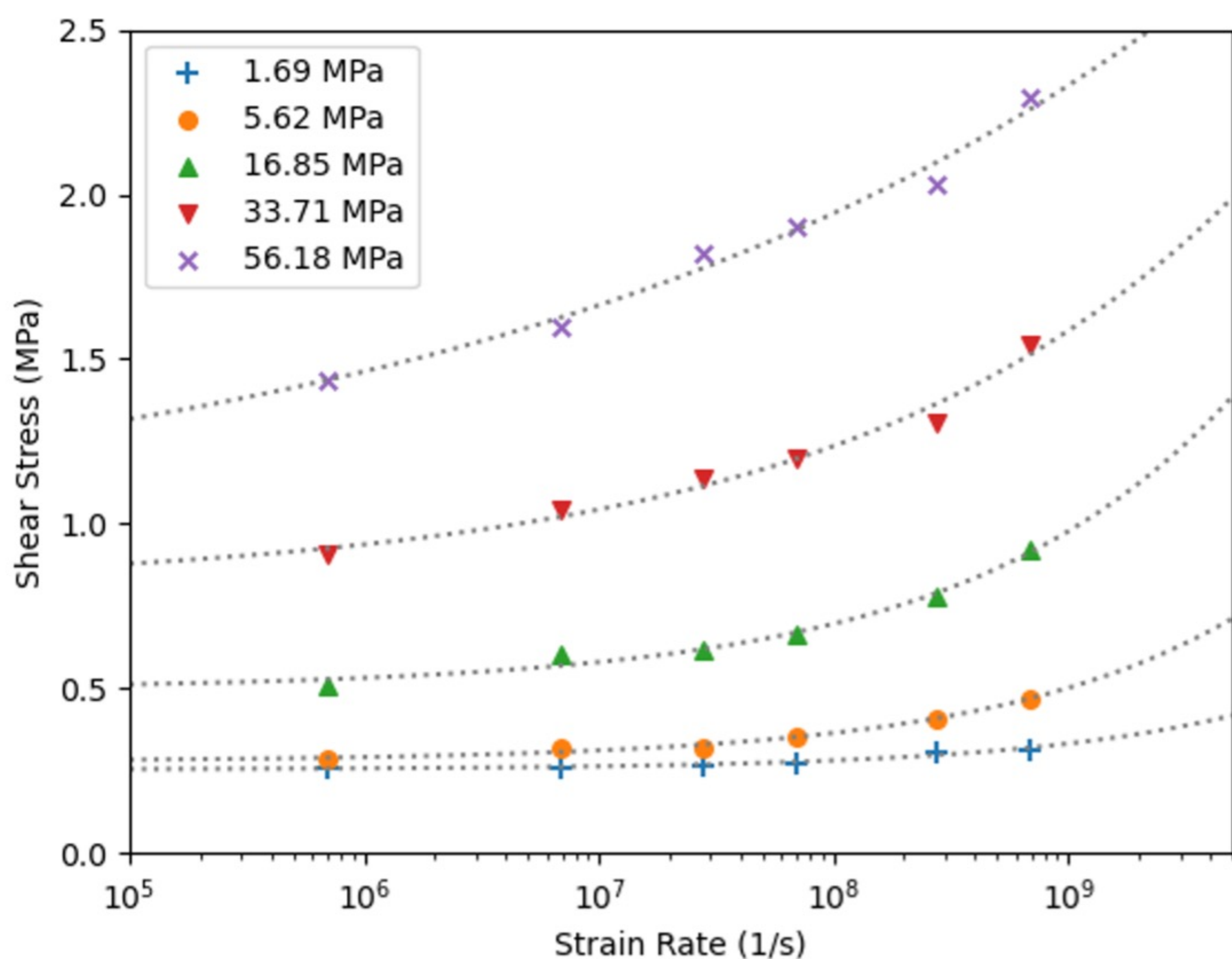


Figure 6.

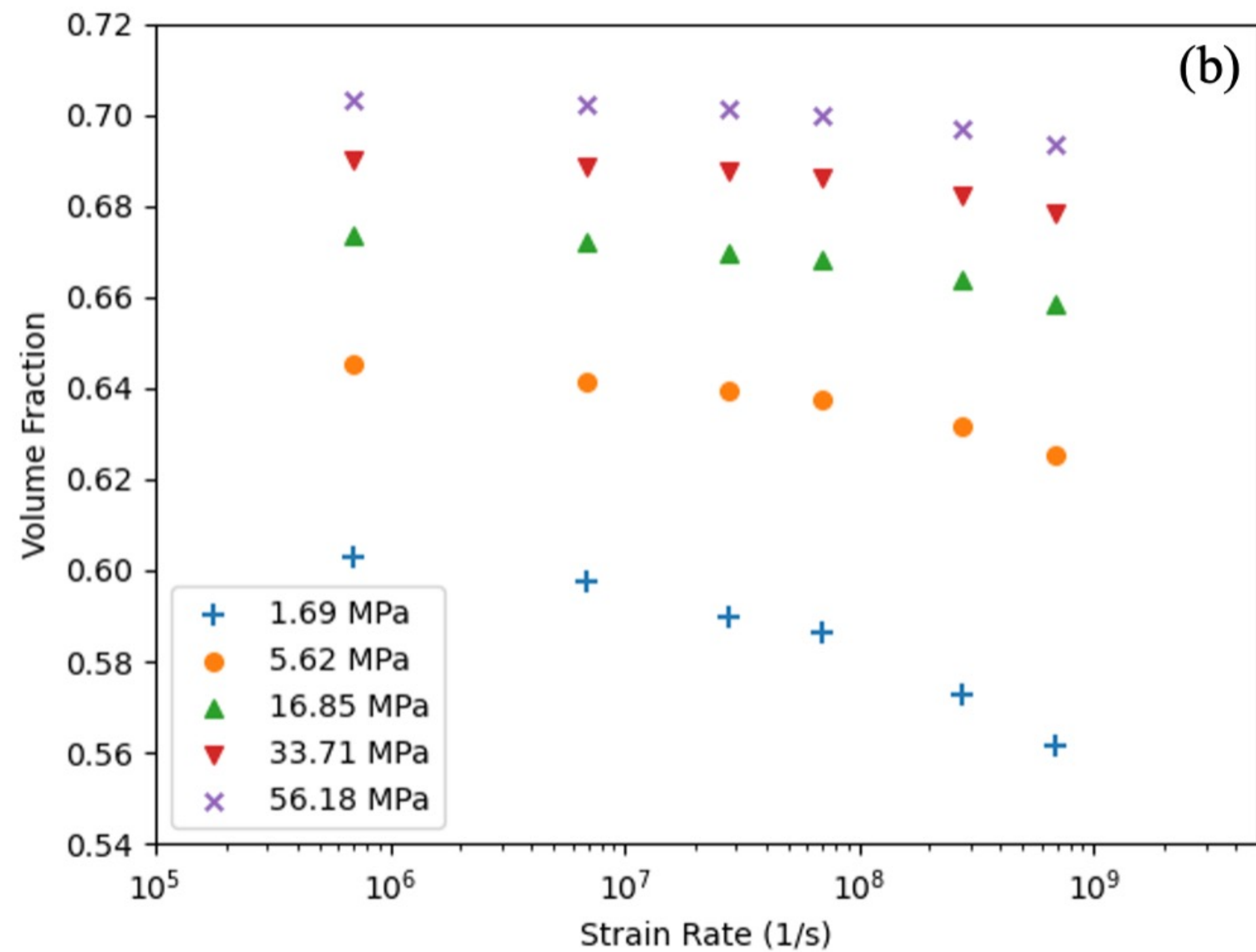
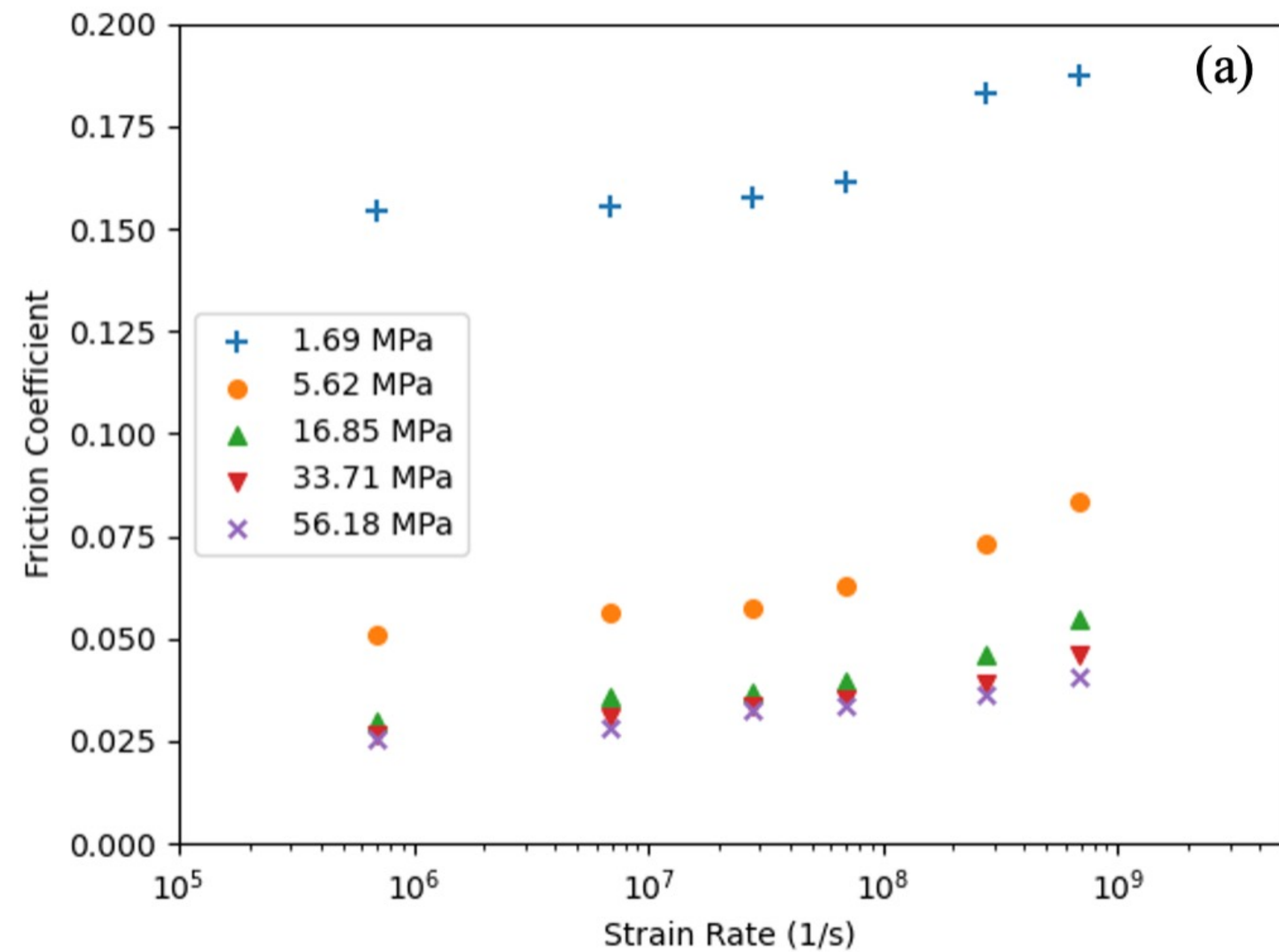


Figure 7.

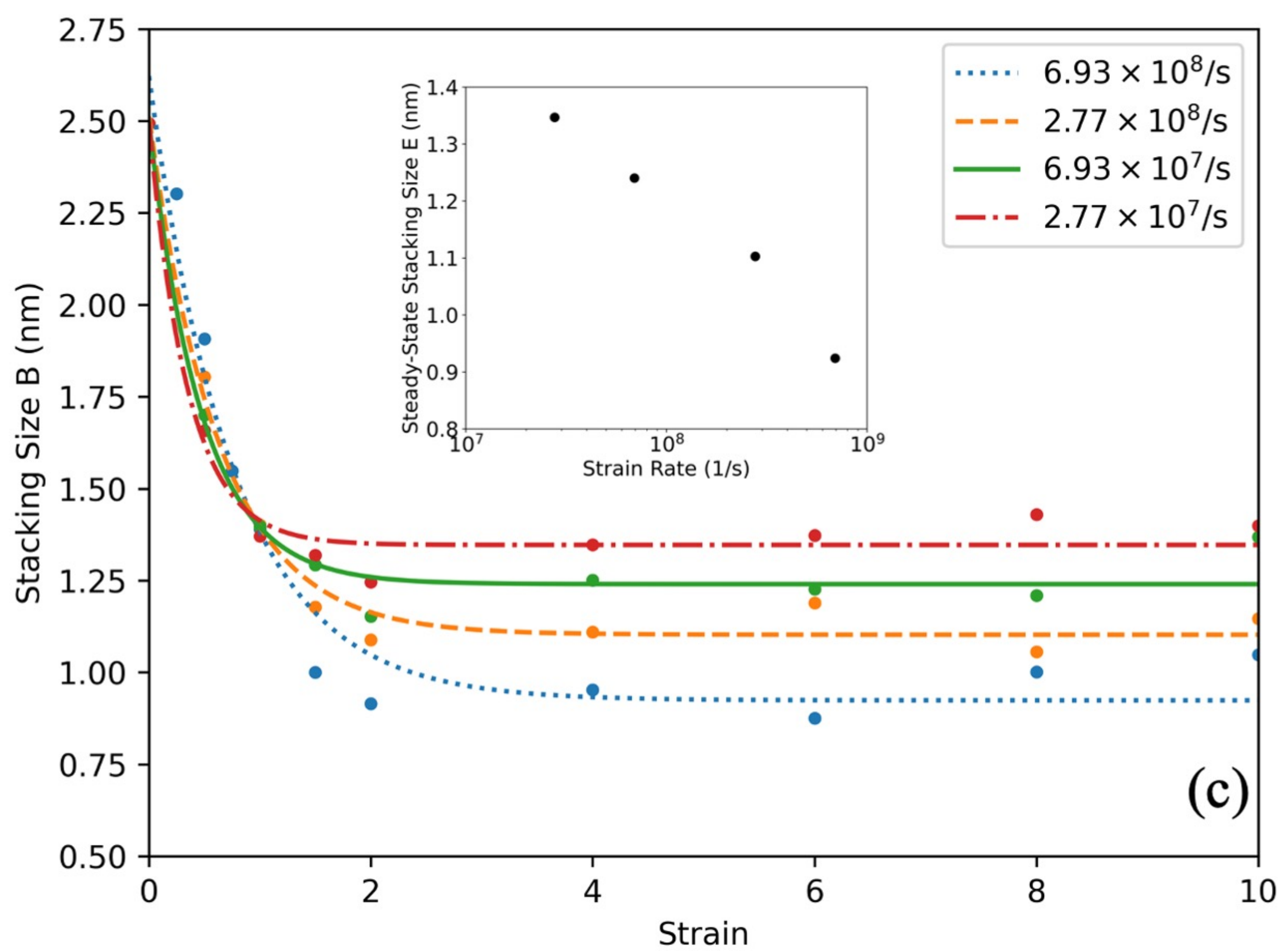
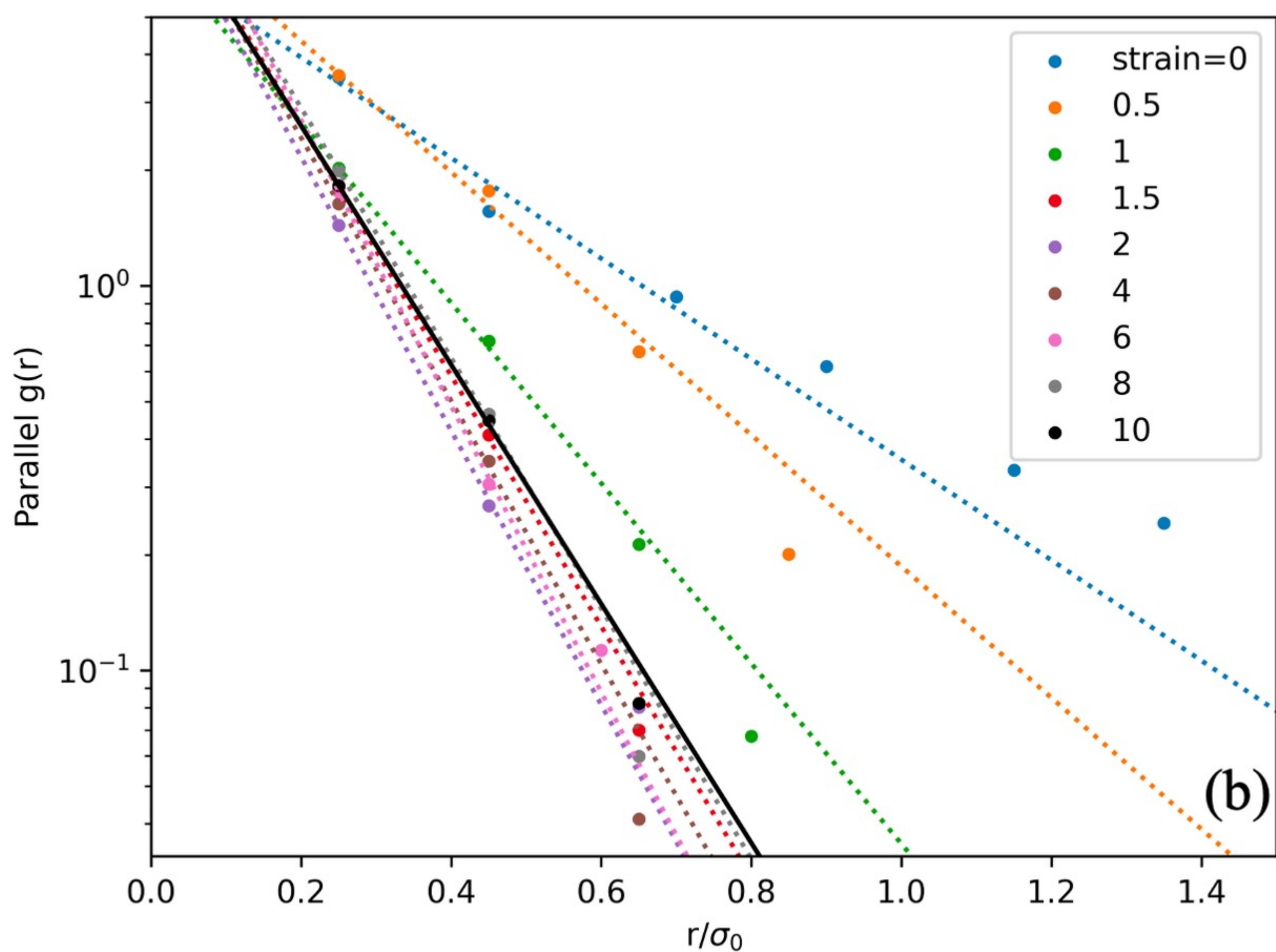
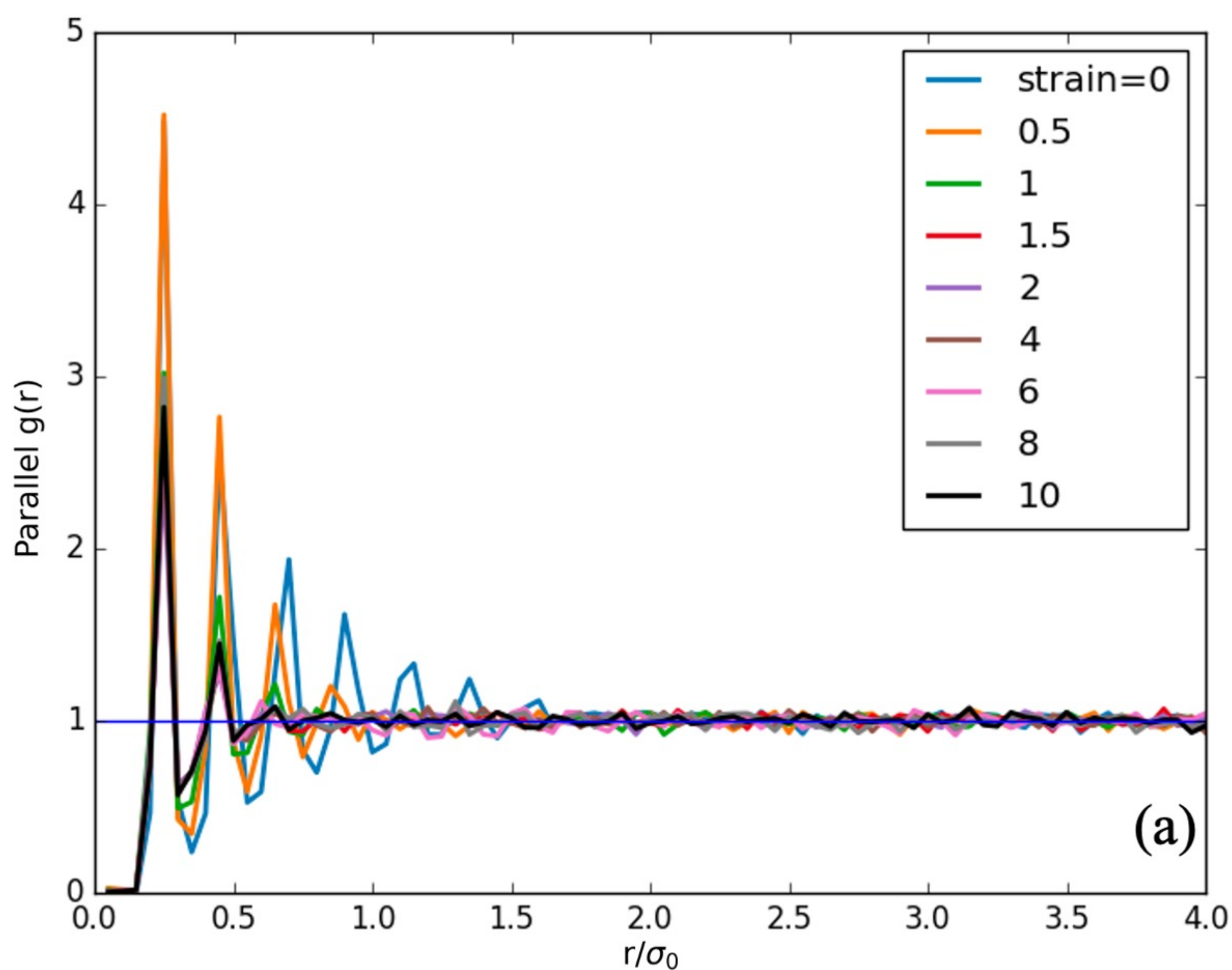


Figure 8.

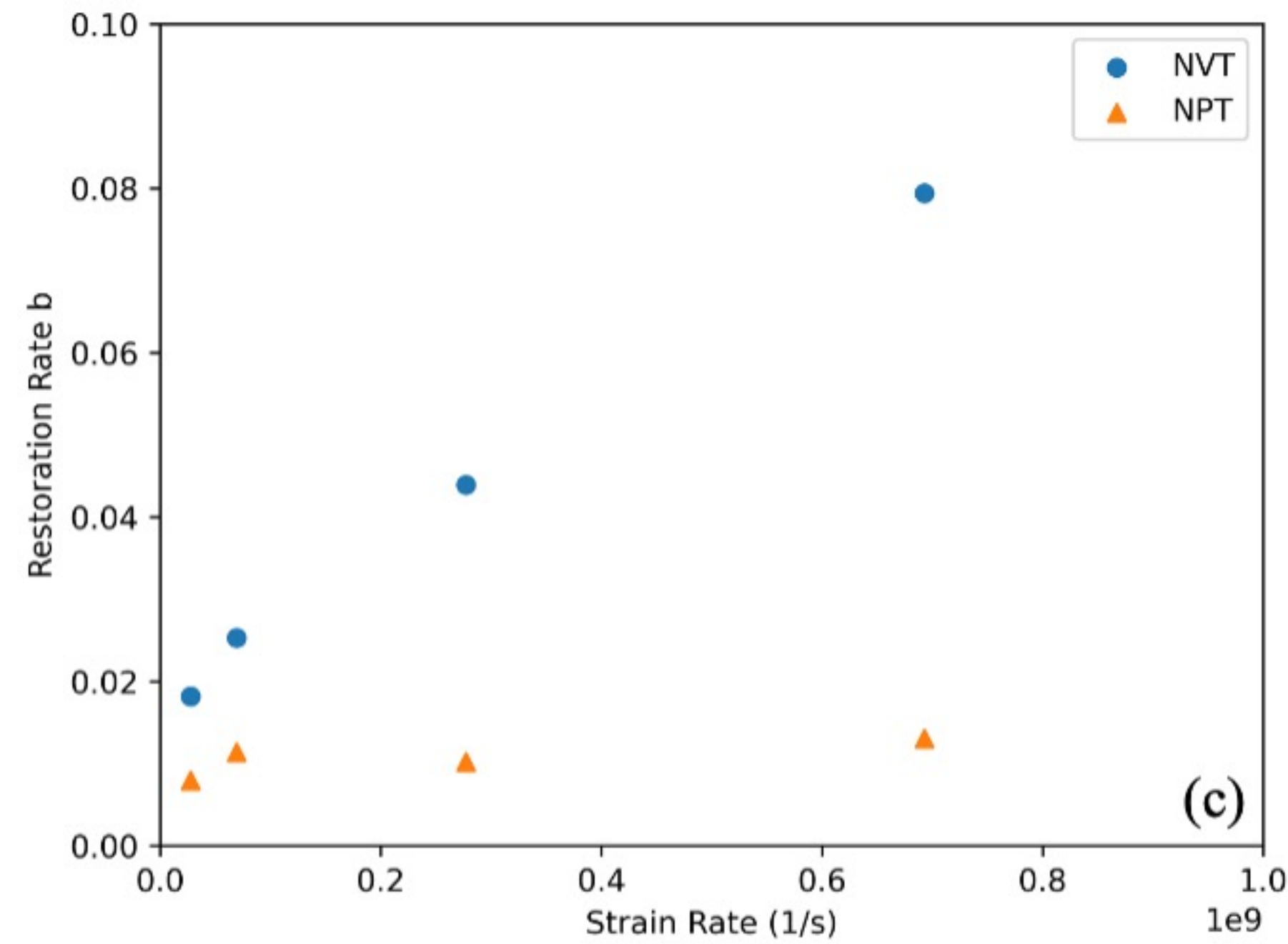
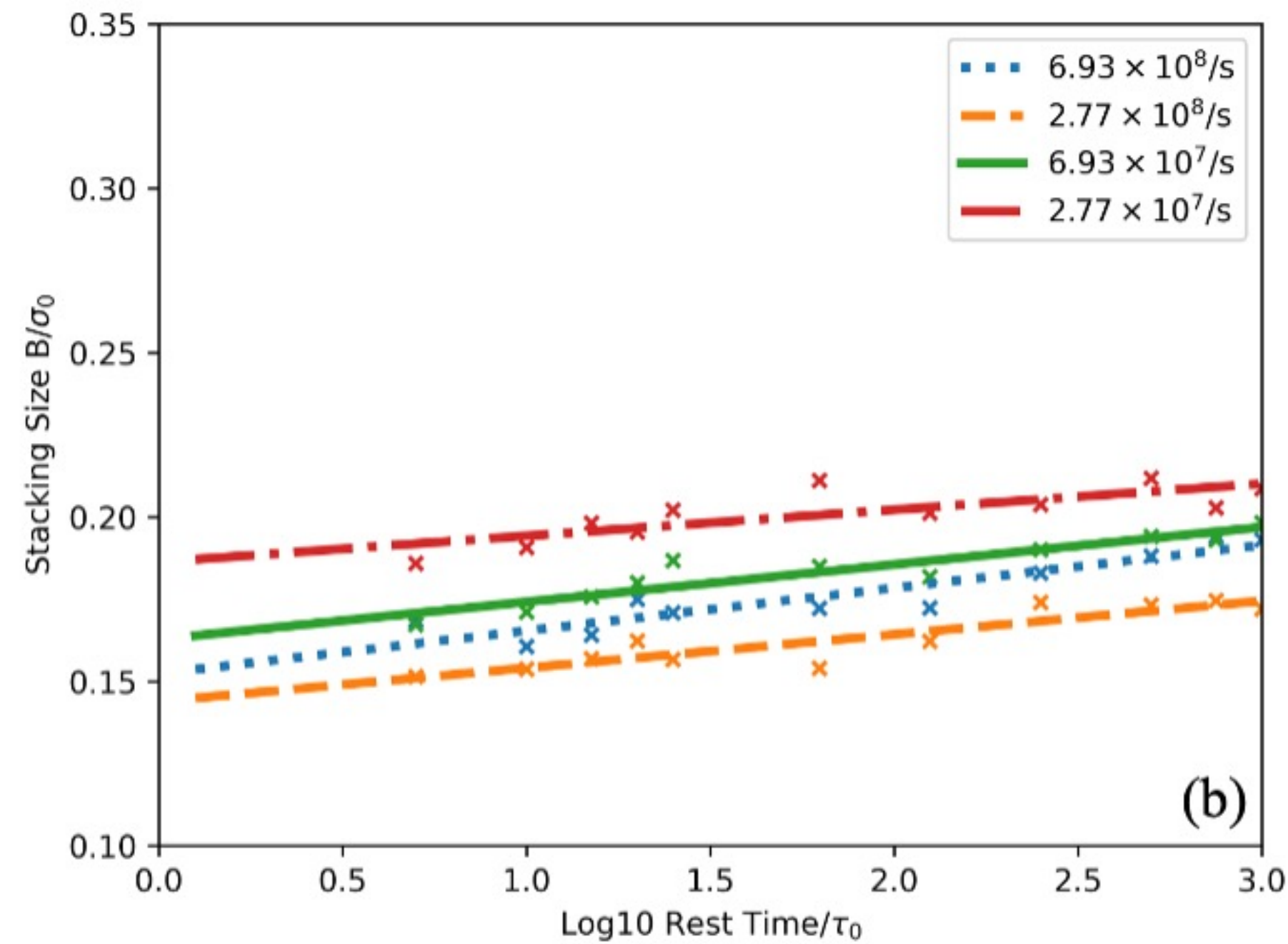
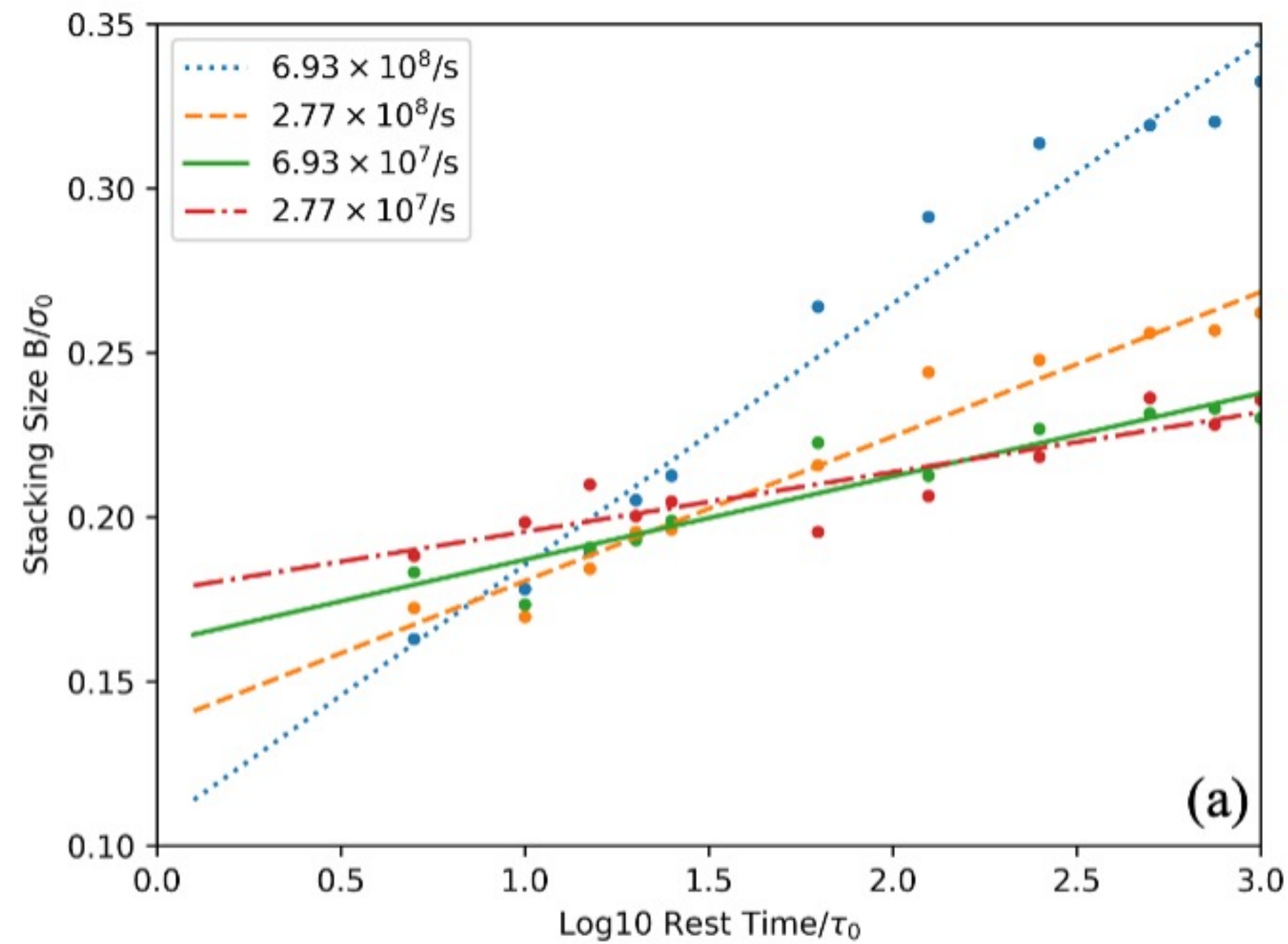
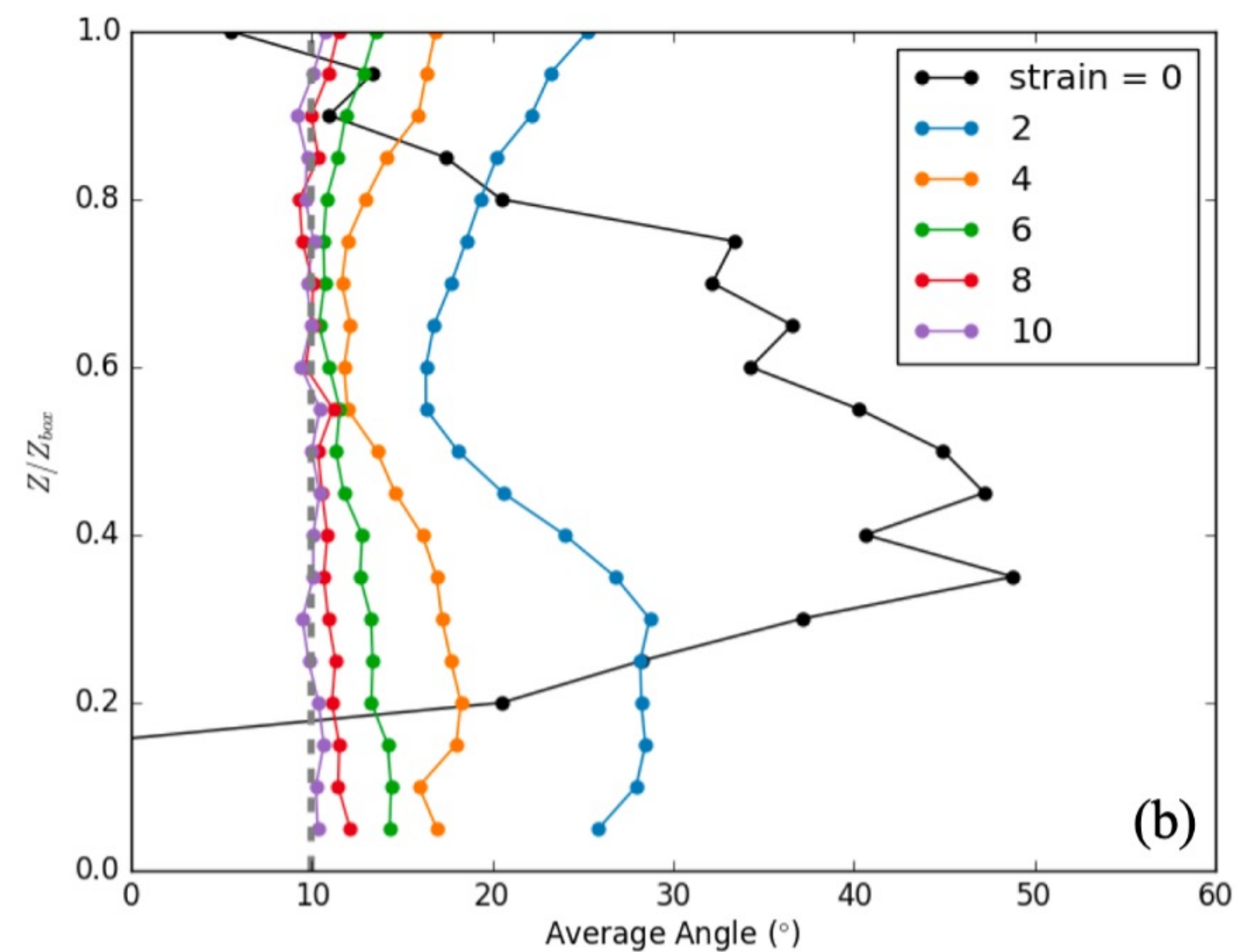
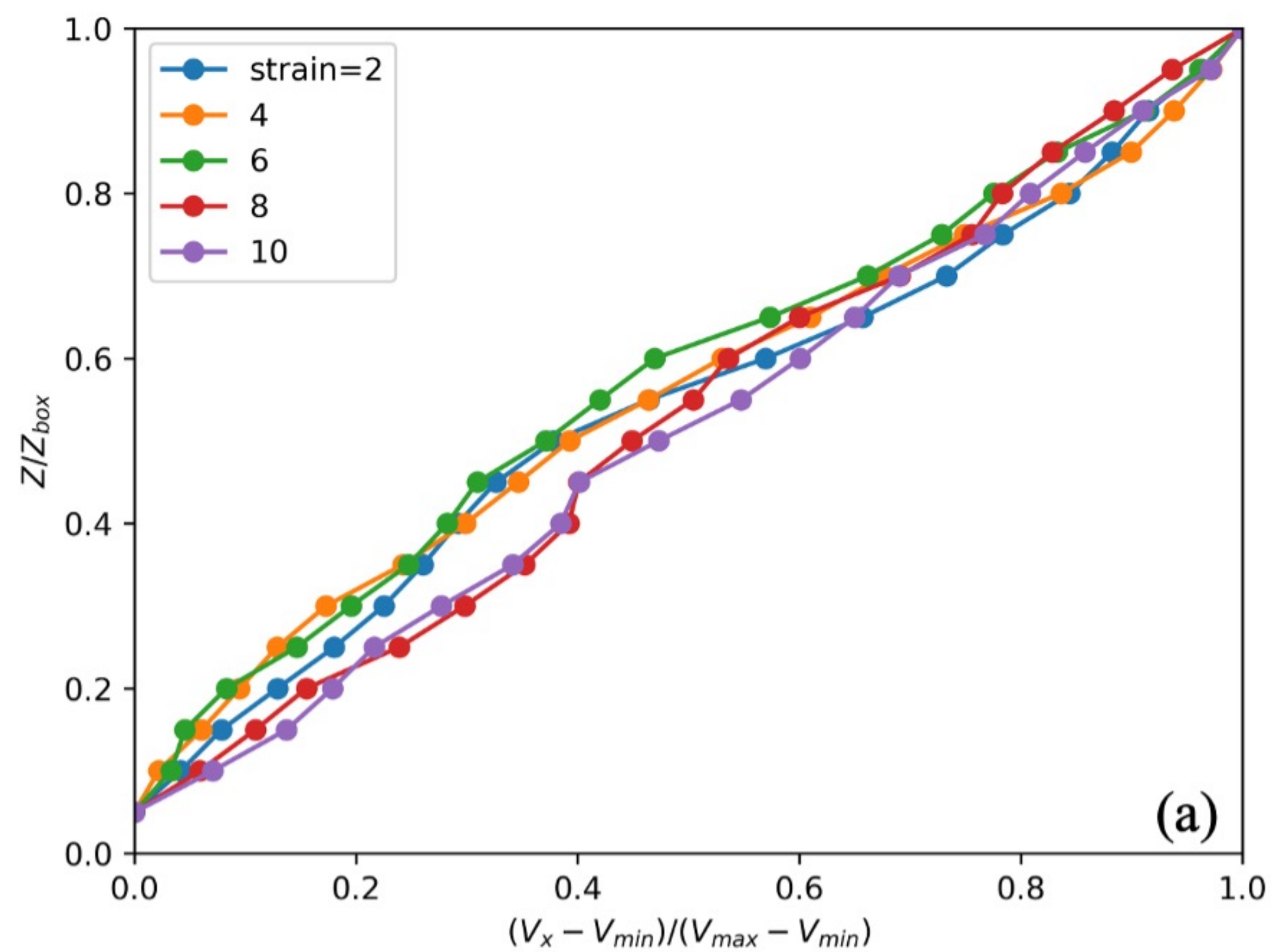


Figure 9.

$\dot{\gamma}=2.77 \times 10^7$ /s
Homogeneous



$\dot{\gamma}=6.93 \times 10^6$ /s
Shear band

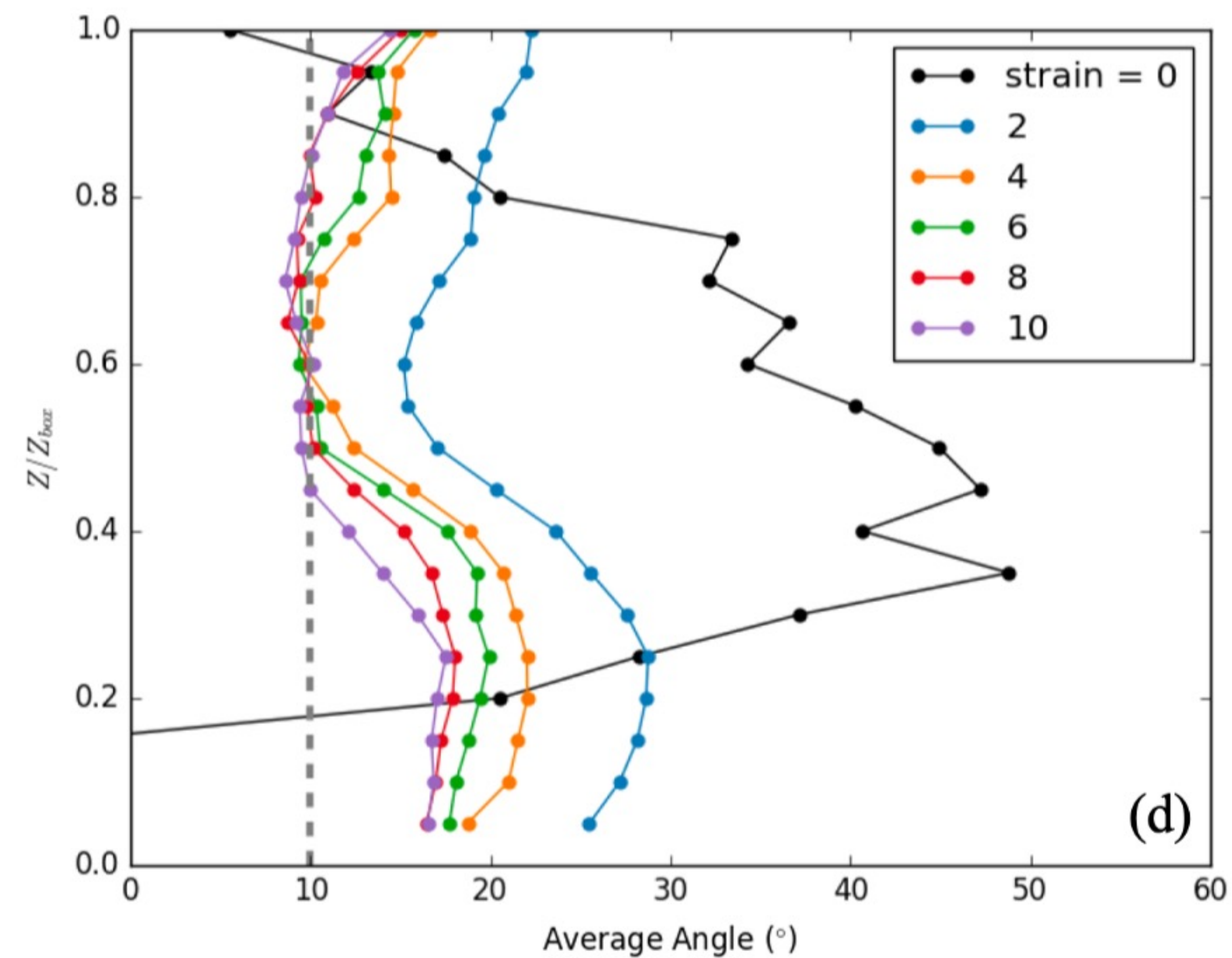
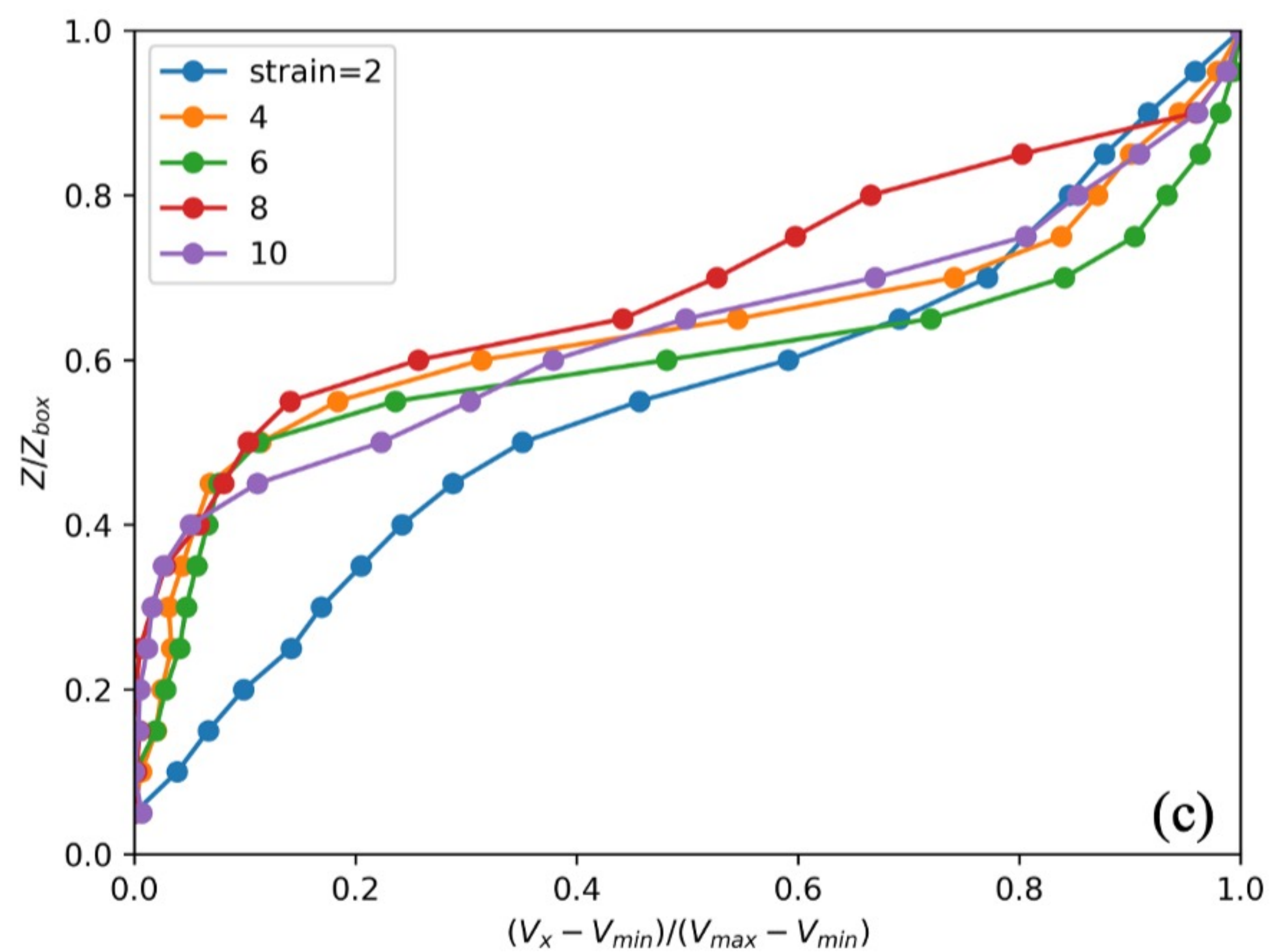


Figure 10.

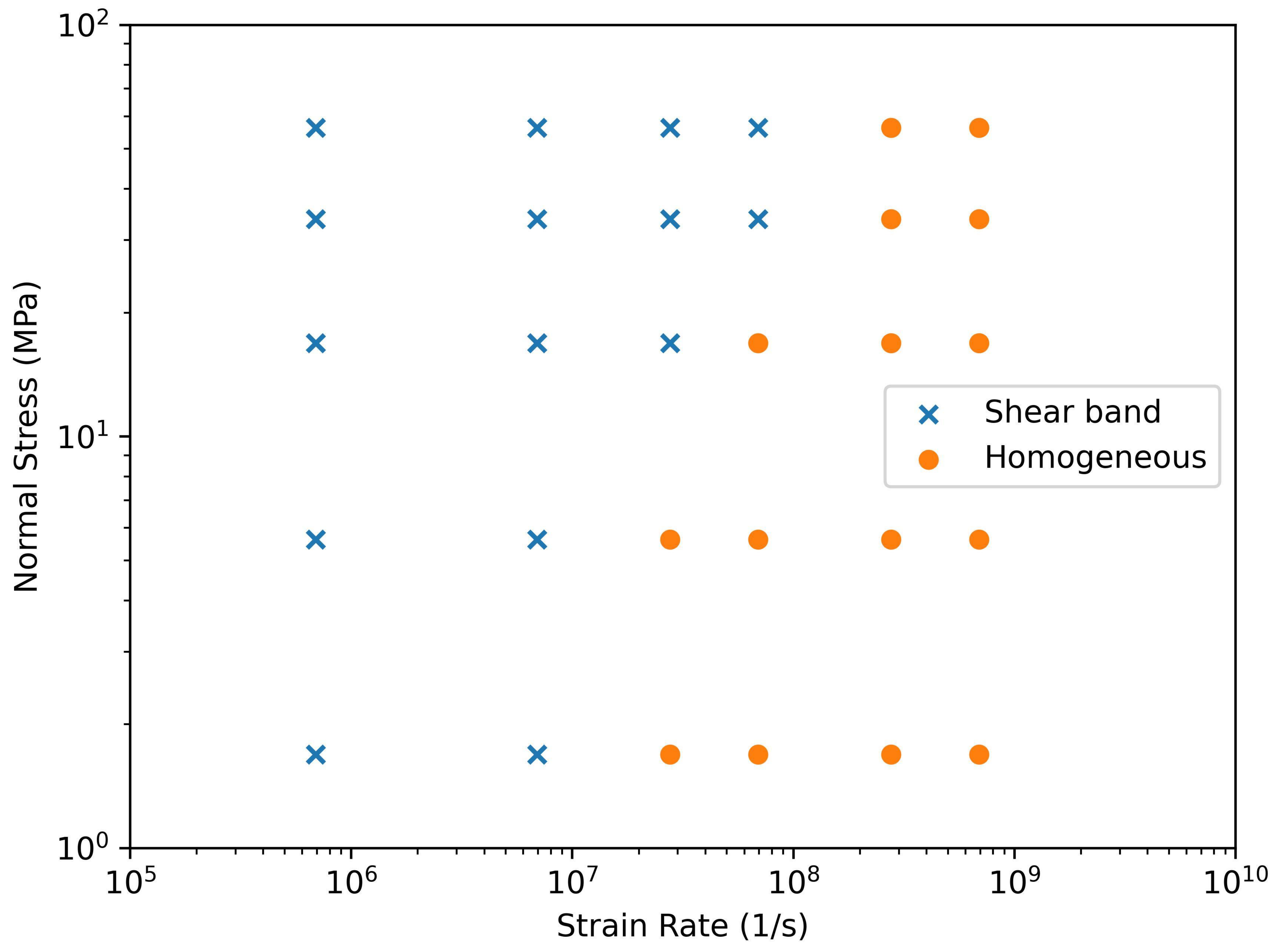
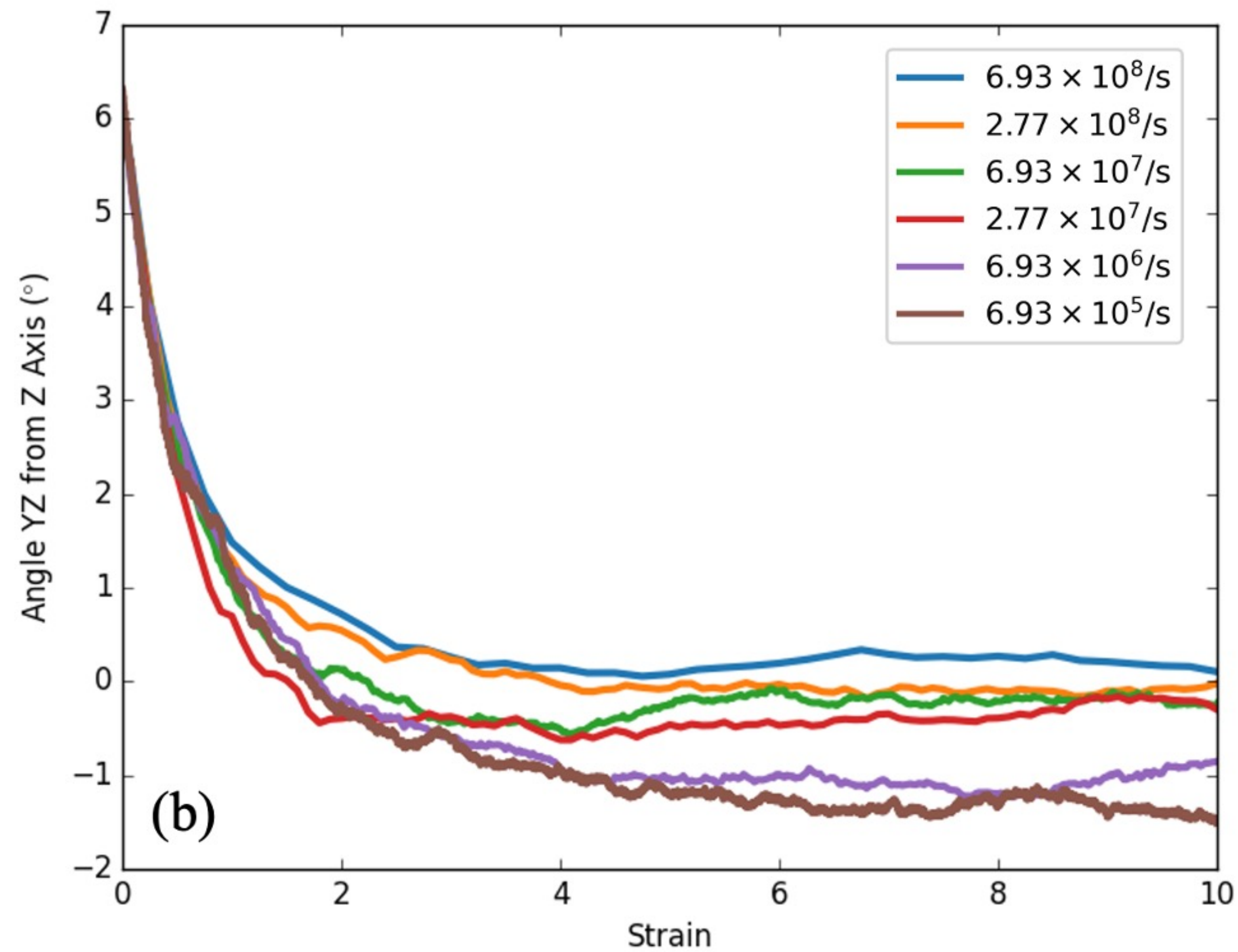
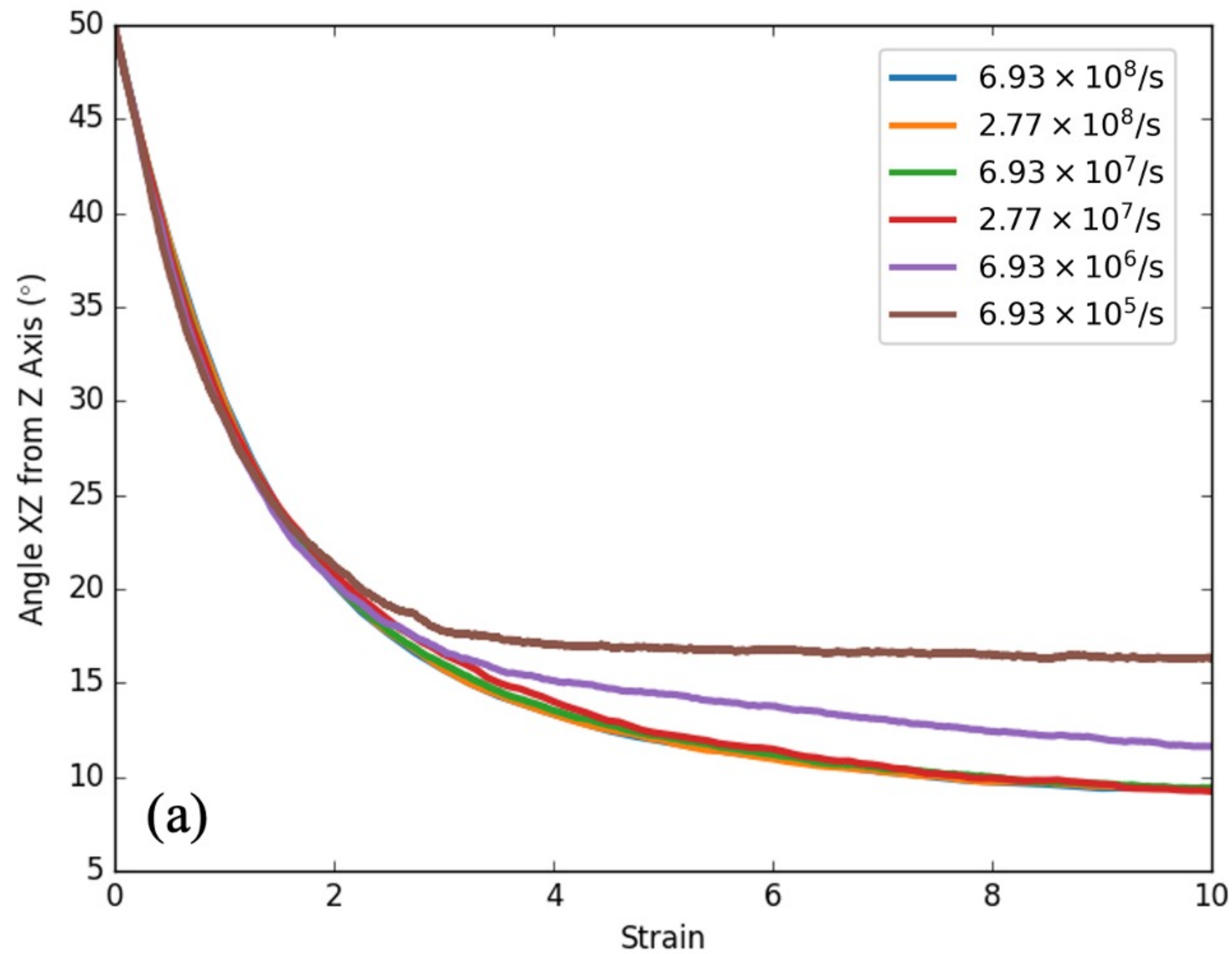


Figure 11.



Rheology and Structure of Model Smectite Clay: Insights from Molecular Dynamics

Z.-Y. Lin¹ and T. Hatano¹

¹Department of Earth and Space Science, Osaka University, Osaka, Japan

Contents of this file

Text S1

Tables S1 to S4

Introduction

This supplementary file includes a brief description of the Gay-Berne potential used to describe clay interaction in our model. We have also included four tables on all the fitting parameters used in the data analysis.

Text S1.

Gay-Berne Potential

The Gay-Berne potential is used to describe the interaction between clay platelets with shape and energy anisotropy. Each clay platelet is treated as an effective oblate ellipsoid. Then the pair potential is in the form (Coussaert and Baus, 2002; Gay and Berne, 1981; Luckhurst and Simmonds, 1993):

$$V(\mathbf{r}_{12}, \mathbf{u}_1, \mathbf{u}_2) = \epsilon_0 \epsilon(\mathbf{u}_1, \mathbf{u}_2, \hat{\mathbf{r}}_{12}) \times \varphi\left(\frac{r_{12}}{\sigma_0} + 1 - \sigma(\mathbf{u}_1, \mathbf{u}_2, \hat{\mathbf{r}}_{12})\right) \quad (\text{S1})$$

where $\hat{\mathbf{r}}_{12}$ is the unit vector along the center-to-center vector \mathbf{r}_{12} between two particles, $r_{12} = |\mathbf{r}_{12}|$. \mathbf{u}_1 and \mathbf{u}_2 are unit vectors along the symmetry axis of particle 1 and 2. ϵ_0 and σ_0 set the energy and length scale. $\varphi(y) = y^{12} - y^6$ is the dimensionless 12-6 Lennard-Jones potential.

Each function in Eq. (S1) is chosen as:

$$\sigma(\mathbf{u}_1, \mathbf{u}_2, \hat{\mathbf{r}}_{12}) = \left\{ \left(\frac{1+\chi}{1-\chi} \right) w(\mathbf{u}_1, \mathbf{u}_2, \hat{\mathbf{r}}_{12}; \chi) \right\}^{-1/2} \quad (\text{S2})$$

$$w(\mathbf{u}_1, \mathbf{u}_2, \hat{\mathbf{r}}_{12}; \chi) = 1 - \frac{\chi}{2} \left\{ \frac{(\hat{\mathbf{r}}_{12} \cdot (\mathbf{u}_1 + \mathbf{u}_2))^2}{1 + \chi \mathbf{u}_1 \cdot \mathbf{u}_2} + \frac{(\hat{\mathbf{r}}_{12} \cdot (\mathbf{u}_1 - \mathbf{u}_2))^2}{1 - \chi \mathbf{u}_1 \cdot \mathbf{u}_2} \right\} \quad (\text{S3})$$

$$\epsilon(\mathbf{u}_1, \mathbf{u}_2, \hat{\mathbf{r}}_{12}) = \{1 - \chi^2 (\mathbf{u}_1 \cdot \mathbf{u}_2)^2\}^{-\nu/2} \times w(\mathbf{u}_1, \mathbf{u}_2, \hat{\mathbf{r}}_{12}; \chi')^\mu \quad (\text{S4})$$

The zeros of the potential are determined by Eqs. (S2) and (S3). The anisotropy of the Gay-Berne potential is captured by the powers of ν and μ in Eq. (S4), where the first factor on the right-hand side favors alignment in the direction parallel to the symmetry axis.

For discotic molecules, we follow the convention to use $\nu = 2$ and $\mu = 1$ (Caprion et al., 2003; Cienega-Cacerez et al., 2014; Coussaert and Baus, 2002). The aspect ratio $\kappa = \sigma_{ff}/\sigma_{ee}$ is the ratio of particle thickness (face-to-face) to particle diameter (end-to-end), $\kappa < 1$ corresponds to a discotic molecule and $\kappa = 1$ corresponds to spherical molecule. The energy ratio $\kappa' = \epsilon_{ee}/\epsilon_{ff}$ is the ratio of the corresponding well depth between the end-to-end configuration and the face-to-face configuration, then:

$$\chi = \frac{\kappa^2 - 1}{\kappa^2 + 1}, \chi' = \frac{\kappa' - 1}{\kappa' + 1}, \epsilon_0 = (1 - \chi^2) \epsilon_{ee}, \sigma_0 = \sigma_{ff} = \kappa \sigma_{ee} \quad (\text{S5})$$

The system considered in this work are mixtures of three type of particles A, B and C with the same thickness and different diameter, corresponding to aspect ratio κ of 1/5, 1/6 and 1/7. The slight polydispersity is introduced to avoid crystallization in mono-dispersed system. The type with the smallest aspect ratio (1/5) is used as a reference component with mass $m_A = 1$ and diameter $\sigma_{A,ff} = \sigma_0 = 1$. The energy ratio $\kappa' = 1/5$ is used for all particles.

For interaction between different particle types, the following mixing rule is used after Cienega-Cacerez et al. (2016):

$$\epsilon_{ij} = \sqrt{\epsilon_i \epsilon_j}, \sigma_{ij} = \frac{\sigma_i + \sigma_j}{2} \quad (\text{S6})$$

Table S1. Fitting parameters of the Herschel-Bulkley model of shear stress dependence on strain rate in Figure 5a.

Table S2. Fitting parameters of the exponential model of PaRDF peak dependence on distance, an example at normal stress $P = 5.62 \text{ MPa}$ and strain rate $\dot{\gamma} = 6.93 \times 10^8 / \text{s}$ in Figure 7b.

Table S3. Fitting parameters of the exponential model of stacking size dependence on shear strain at normal stress $P=5.62\text{MPa}$ in Figure 7c.

Table S4. Fitting parameters in Equation (7) at normal stress $P = 5.62 \text{ MPa}$ in Figure 8.

Table S1. Fitting parameters of the Herschel-Bulkley model of shear stress dependence on strain rate in Figure 5a.

Normal stress (MPa)	Herschel-Bulkley model			
	τ_0	K	n	R2
1.69	0.254	5.97×10^{-6}	0.458	0.9390
5.62	0.278	4.32×10^{-5}	0.413	0.9933
16.85	0.498	1.70×10^{-4}	0.383	0.9837
33.71	0.807	3.63×10^{-3}	0.259	0.9781
56.18	0.944	7.25×10^{-2}	0.142	0.9820

Table S2. Fitting parameters of the exponential model of PaRDF peak dependence on distance, an example at normal stress $P = 5.62 \text{ MPa}$ and strain rate $\dot{\gamma} = 6.93 \times 10^8 \text{ /s}$ in Figure 7b.

Shear strain	Exponential model		
	A	B	R2
0	7.164	2.493	0.9806
0.5	9.512	1.907	0.9932
1.0	7.809	1.390	0.9988
1.5	11.698	1.001	0.9997
2.0	11.137	0.915	0.9993
4.0	11.724	0.952	0.9993
6.0	14.965	0.876	0.9995
8.0	12.982	1.001	0.9991
10.0	10.903	1.048	0.9996

Table S3. Fitting parameters of the exponential model of stacking size dependence on shear strain at normal stress $P=5.62\text{MPa}$ in Figure 7c.

Strain rate (1/s)	Exponential model			
	C	D	E	R2
6.93×10^8	1.698	0.764	0.924	0.9654
2.77×10^8	1.409	0.636	1.103	0.9864
6.93×10^7	1.257	0.478	1.240	0.9793
2.77×10^7	1.150	0.351	1.347	0.9777

Table S4. Fitting parameters in Equation (7) at normal stress $P = 5.62 \text{ MPa}$ in Figure 8.

Previous strain rate (1/s) (NVT rest)	Logarithmic model		
	a	b	R2
6.93×10^8	0.106	0.079	0.9664
2.77×10^8	0.137	0.044	0.9605
6.93×10^7	0.162	0.025	0.8861
2.77×10^7	0.177	0.182	0.7936
(NPT rest)			
6.93×10^8	0.152	0.013	0.8436
2.77×10^8	0.144	0.010	0.8149
6.93×10^7	0.163	0.011	0.8689
2.77×10^7	0.186	0.008	0.6150